# Molecular model of a bacterial flagellar motor *in situ* reveals a "parts-list" of protein adaptations to increase torque

Tina Drobnič[1,2,3,£], Eli J. Cohen[1,4,£], Mona Alzheimer[5,6], Kathrin Froschauer[5,7], Sarah Svensson[5,8,9], Nanki Singh[1], Sriram G. Garg[10,11], Louie Henderson[1,12], Trishant Umrekar[1], Andrea Nans[13,14], Deborah Ribardo[15], Georg Hochberg[11], David R. Hendrixson[15,16], Cynthia M. Sharma[5,17], Peter Rosenthal[18,19], Morgan Beeby[1,20,*]

[1]Department of Life Sciences, Imperial College London, London, SW7 2AZ, UK

[2]ORCID: 0000-0001-6364-1874

[3]Tina Drobnič current affiliation: MRC Laboratory of Molecular Biology, Cambridge CB2 0QH, UK.

[4]ORCID: 0000-0001-9265-7517

[5]University of Würzburg, Institute of Molecular Infection Biology, Department of Molecular Infection Biology II, Josef-Schneider-Straße 2/D15, 97080 Würzburg, Germany

[6]ORCID: 0000-0002-0094-3987

[7]ORCID: 0000-0001-5288-4440

[8]Current affiliation: The Center for Microbes, Development and Health, CAS Key Laboratory of Molecular Virology and Immunology, Institut Pasteur of Shanghai, Chinese Academy of Sciences, Shanghai, China 200031. email: sarah.svensson@ips.ac.cn

[9]ORCID: 0000-0002-3183-6084

[10]ORCID 0000-0003-4160-5228

[11]Max Planck Institute for Terrestrial Microbiology, Marburg, Germany

[12]Current affiliation: Peptone Ltd, 370 Grays Inn Road, London WC1X 8BB, UK

[13]Structural Biology Science Technology Platform, The Francis Crick Institute, London NW1 1AT, UK

[14]ORCID: 0000-0002-3791-2447

[15]Department of Microbiology, University of Texas Southwestern Medical Center, Dallas, TX 75390

[16]ORCID: 0000-0001-8496-2466

[17]ORCID: 0000-0002-2321-9705

[18]Structural Biology of Cells and Viruses Laboratory, The Francis Crick Institute, London NW1 1AT, UK

[19]ORCID: 0000-0002-0387-2862

[20]ORCID: 0000-0001-6413-9835

[£] These authors contributed equally to this work

[*]Correspondence: mbeeby@imperial.ac.uk

# Abstract

One hurdle to understanding how molecular machines function and evolve is our inability to see their structures *in situ*. Here we describe a minicell system that enables *in situ* cryogenic electron microscopy imaging and single particle analysis to probe the mechanisms and evolution of an iconic molecular machine, the bacterial flagellar motor, which spins a helical propeller for bacterial propulsion. Innovations in sample preparation and imaging enabled resolutions sufficient to build an *in situ* molecular model of the *C. jejuni* flagellar motor. Our results provide unprecedented insights into the *in situ* context of flagellar motors, highlight origins of recruited components involved in the unusually high torque of the *C. jejuni* motor, identify previously unknown components, and reveal corresponding modifications of core components. We also visualise structures involved in torque generation and secretion previously recalcitrant to structure determination. This technique will be of broad applicability to other large membrane-residing protein complexes. Note that this manuscript has a sibling manuscript titled "*Evolution of a large periplasmic disk in Campylobacterota flagella facilitated efficient motility alongside autoagglutination*" that dissects the function of the large disk described in this manuscript.

# Introduction

How evolution produces novelty remains a central question in biology. While innovations in eukaryotes often arise by rewiring existing gene transcriptional networks (1), examples of the emergence of evolutionary novelty at the molecular scale remain scarce. The few case studies in the emergence of new molecular structures are limited to small protein complexes (2–5).

Examples of the emergence of novelty in molecular machines are found in bacterial flagella, helical propellers rotated by a cell-envelope-embedded rotary motor (Fig. 1A) (6). The flagellar motor is composed of a ring of inner-membrane motor proteins ("stator complexes") which harness ion flux to rotate a large cytoplasmic rotor ring (the "C-ring"). Torque is transmitted through a chassis (the "MS-ring") and periplasm-spanning axial driveshaft (the "rod") to extracellular universal joint and propeller structures (the "hook" and "flagellar filament", respectively) to generate thrust. While the conserved flagellar core predates the last universal bacterial ancestor, many species have incorporated diverse additional proteins to adapt motor function (7), often scaffolding more than the ~11 stator complexes in *Salmonella enterica* and *Escherichia coli* (8–10). Some of the most structurally complex

motors are found in Campylobacterota, which produce three times higher torque than *E. coli* and *Salmonella*, and includes the pathogens *Campylobacter jejuni* and *Helicobacter pylori* (9,11). Campylobacterota flagellar motors have incrementally incorporated additional proteins (10); one of the most complex motors, that of *C. jejuni*, features a large periplasmic outer membrane-associated basal disk together with a periplasmic scaffold of novel proteins required for incorporation of 17 stator complexes in a wider ring than simpler motors (9). This additional complexity relative to model organisms, together with the motor's size and easy-to-assay motility phenotype, make it ideal for investigating keys steps in motor evolution.

Understanding how and why these additional proteins were incorporated into the motor requires molecular models, but the size, intimate membrane association, and multiple moving parts have hampered structural determination. Cryogenic electron microscopy (cryoEM) subtomogram average structures to between 16 and 18 Å-resolution (12) (13), and structures of purified flagellar motors by single particle analysis cryoEM lacking dynamic components (14,15) cannot answer a number of critical questions, and advance in imaging membrane proteins are restricted to spherical liposomes rather than native context (16,17).

To address these challenges we engineered *C. jejuni* minicells to determine a subnanometre-resolution structure of the flagellar motor *in situ* using single particle analysis. The quality of our map enabled us for the first time to build a near-complete molecular model of an intact flagellar motor in its native context. Our model provides key insights into the functional contributions of recruited proteins, reveals distant homologies based on structural comparisons, identifies previously unknown components, and contextualises adaptations of pre-existing core machinery to these recruited proteins. We also gain insights into the function of the conserved core of the flagellar motor and its integral type III secretion system (T3SS). This first *in situ* structure of such a complex motor suggests a general approach for structural studies of other molecular machines.

# Results

## *Minicell engineering and projection imaging enable subnanometre flagellar motor resolution*

We used a hybrid cryoEM imaging approach to determine the *in situ* structure of the *C. jejuni* flagellar motor. Bacterial cell division can be disrupted to produce flagellated minicells that retain the ability to swim (18). To increase particle number for high-throughput, high-resolution structure determination, we exploited the multiply-flagelled minicells produced by

a Δ*flhG* mutation (19) and deleted flagellar filament components *flaA* and *flaB* for efficient centrifugal purification (Fig. 1B,C). The resulting ~200 nm-diameter minicells are thinner and more homogenous than ~350 nm-diameter minicells from enteric bacteria, enabling us to enrich to >99% minicells for high-throughput imaging (20).

We acquired micrographs of purified minicells for *in situ* single particle analysis. Preliminary processing and 2-D classification revealed major features including the stator complexes and their periplasmic scaffold, basal disk, C-ring, MS-ring, rod, and the integral flagellar type III secretion system (Fig. 1D). Classification and refinement using applied C17 symmetry (9) yielded a whole-motor reconstruction from 32,790 particles to 9.4 Å resolution (Fig. 1E, Fig. S1), improving upon our previous subtomogram averaging structure of 44 Å resolution (9). This structure resolved membranes and protein components (Fig. 1F).Focused refinement of the innermost ring of the basal disk, the periplasmic scaffold, and the embedded stator complexes improved resolution to 7.9 Å (Fig. 2A, Fig. S1D,E,F), sufficient to resolve secondary structure features of most subunits (Fig. 2B). The periplasmic scaffold is composed of the outer membrane-proximal basal disk, the medial disk, and the inner membrane-proximal proximal disk, all of which share a 17-fold symmetry axis. A single asymmetric unit of the 17-fold symmetric periplasmic scaffold revealed that the basal disk is composed of concentric rings (Fig. 2B). The medial disk-facing sides of the first five of these rings featured additional densities whose intensity decreased with ring radius. The medial and proximal disks are 17-fold symmetric proteinaceous lattices with clearly-resolved α-helices, and the periplasmic domain of MotB is evident at the outer radius of the proximal disk (9).

## *The basal disk is composed of concentric rings of FlgP*

To understand structural features of the basal disk, which we previously determined is composed of FlgP and tentatively FlgQ (Fig. 2C). The disk is sufficiently rigid to push the outer membrane away from the inner membrane at increasing distances from the rotational axis of the motor, consistent with our previous observation that the disk retains its distinct shape even after deletion of other parts of the periplasmic scaffold (9). Our density map revealed concentric rings; the innermost ring shared the 17-fold symmetry of the medial and proximal disks, with 17 trimeric repeats of 51 protomers. One protomer from each trimeric repeat featured the additional densities that face the medial disk described above (Fig. 2B), suggesting the 17 trimers template the overall 17-fold symmetry of the other periplasmic structures. We predicted the structure of the major protein component of the basal disk, FlgP (9), in monomeric and multimeric forms, excluding the N-terminal 65-residue signal sequence and disordered linker using AlphaFold (21) (Fig S2A). The FlgP monomer folds as

a modified SHS2 domain with a core α-helix and three-stranded β-sheet in a βαββ topology similar to flavoprotein dodecin (22) (Fig S2A,D). Structural searches revealed that FlgP shares this fold with *Helicobacter* protein Lpp20 (23) (top Dali (24) hit, reported RMSD 2.1 Å) (Fig. 2J). FlgP is further modified with a short C-terminal helix and a long β-hairpin between the α-helix and second β-sheet that extends 35 Å at a ~42° angle to the vertical axis (Fig S2A). Structural predictions of FlgP oligomers suggested that this β-hairpin forms a smooth continuous β-sheet with lateral association of one FlgP to the next two protomers. Arcs of these interlocked FlgP oligomers fitted well into our density map, with 51 protomers forming the complete innermost basal disk ring (Fig. 2C,E, Fig S2E). Although we could not discern the symmetries of subsequent concentric rings, they have comparable cross-sections, and we modelled them as rings of FlgP by inferring their subunit number based on ratios of circumferences (Fig 2B,C).

FlgQ occurs in an operon with FlgP, is outer membrane-localized, and required for FlgP stability (21). We found that its predicted structure resembles a two-protomer repeat of FlgP (Supplemental Fig S2B). To clarify the location of FlgQ location in the disk we fused an mCherry tag to FlgQ and determined a subtomogram average structure. The structure, however, was indistinguishable from the WT motor (Supplemental Fig. S2C), and we surmise that FlgQ is a low-abundance or irregular component of the disk, or an assembly chaperone.

The basal disk is adjacent to the outer rim of the P-ring of the LP-ring complex (Fig. 1F). Due to comparable diameters of the LP-ring complexes and distal rods of *C. jejuni* and *Salmonella,* and lack of substantial insertions or deletions in corresponding protein sequences, we surmise that the *C. jejuni* LP-ring complex shares the 26-fold symmetry of that in *Salmonella* (14,15). We did not model YecR, which in *Salmonella* caps the L-ring, because we could neither discern a likely protein density atop the L-ring nor find a *C. jejuni* homolog (14). In an accompanying manuscript we show that the basal disk can assemble despite being pushed away from the P-ring, indicating that it does not directly interface with the P-ring despite assembling at a corresponding axial height.The medial disk is composed of lattice of previously unidentified PflC

The identity of the medial disk between the proximal disk and basal disk remained unclear. An unpublished Tn-seq based infection screen from our lab using *C. jejuni* NCTC11168 (Alzheimer, Svensson, Froschauer, Sharma, in preparation) revealed two new proteins, encoded by Cj1643 and Cj0892c, that were required for motility and localised to the cell poles, but did not abolish flagellar filament assembly, suggesting them as possible motor components. Co-immunoprecipitation with proximal disk component PflA in *C. jejuni* 81-176

171 recovered the Cj1643 homolog CJJ81176_1634 and Cj0892c homolog CJJ81176_0901
172 (Table S1). Henceforth we refer to these proteins as PflC and PflD (Paralysed flagellum C
173 and D), respectively. Subtomogram average structures of deletion mutants in *C. jejuni*
174 NCTC11168 revealed loss of the proximal and medial disks upon deletion of *pflC* and loss of
175 a peripheral cage-like structure bridging the outer radii of the medial and proximal disks upon
176 deletion of *pflD* (Fig. 2D).

177 PflC is a 364-residue periplasmic protein predicted to have two domains separated by a
178 proline-rich linker. It features a fold similar to trypsin-like HtrA serine proteases (Fig. 2K)
179 (25). The N-terminal region $PflC_N$, (residues 16-252) contains a serine protease domain and
180 a PDZ-like domain (PDZ1). Separated by a proline-rich linker, C-terminal $PflC_C$ (residues
181 265-364) features a second PDZ-like domain (PDZ2). We found that 17 copies of PflC fit
182 well into the densities projecting beneath each third FlgP subunit of the first basal disk ring,
183 with $PflC_C$ binding FlgP and $PflC_N$ forming the inner band of the medial disk. A density likely
184 to be the ordered proline linker bridges adjacent PflC protomers. This indicates that the $PflC_C$
185 domain of one chain assembles with the $PflC_N$ domain of another, producing a continuous
186 daisy-chain of $PflC_C$ protomers (Fig. 2E). Pulldowns using FLAG-tagged PflC verified its
187 interaction with FlgP (Fig. S3A).

188 PDZ domains interface with binding partners via a hydrophobic pocket using β-strand
189 addition, but $PflC_C$ interactions are evidently mediated by non-canonical PDZ binding (26).
190 The PDZ2 ligand-binding groove is filled by a β-strand from its own polypeptide chain, is
191 oriented away from FlgP, and lacks the conserved PDZ-ligand-binding loop (27). Instead, a
192 loop on the opposite side of the domain comes closest to FlgP. $PflC_N$ contacts other scaffold
193 components, including PflA. The substrate-binding pockets of the protease-like and PDZ1
194 domains are not proximal to other flagellar proteins, suggesting that their interactions are
195 also mediated by non-canonical binding modes.

196 The remainder of the medial disk is an intricate lattice of α-helical densities. The well-
197 resolved secondary structures in this region enabled an exhaustive search with the predicted
198 structures of all *C. jejuni* periplasmic proteins. Our search indicated that this lattice is
199 composed of additional $PflC_N$ subunits related by three dimerisation interfaces (Fig 2F, Fig
200 S4A). An asymmetric unit within this 17-fold symmetric lattice contains six additional $PflC_N$,
201 which we refer to as $PflC_{2\text{-}7}$. Five of these six protomers ($PflC_{2\text{-}6}$) form radial spokes with a
202 slight twist, while $PflC_7$ bridges between spokes. As with $PflC_1$, the C-terminal domains of
203 $PflC_{2\text{-}7}$ explain the densities on the underside of the basal disk (opaque purple density in 2B).

Our structure predicts that purified PflC would oligomerise *ex situ*. We heterologously expressed and purified PflC in *E. coli*. Size exclusion chromatography (SEC) (Fig. S5A,B) and mass photometry measurements (Fig. S5C) revealed a dimer. The *in situ* $PflC_N$-$PflC_C$ daisychaining suggests that the two domains of some PflC polypeptides might also self-associate, reducing the abundance of the dimer. To test this we removed $PflC_C$ (residues 236-349) to yield $PflC_N$ alone. $PflC_N$ produced dimers that were more abundant than $PflC_{NC}$ dimers (Fig. S5D,E,F), supporting an inter-$PflC_N$ interaction. We speculate that interaction of $PflC_N$ and $PflC_C$ from the same polypeptide prevents cytoplasmic oligomerization, and binding of $PflC_C$ to the basal disk catalyzes assembly of the medial disk only in the context of the assembled motor.

The second candidate medial disk component, PflD, is a 162-residue periplasmic protein that was pulled down with PflA of the proximal disk (Table S1). Together with its polar localization (Alzheimer, Svensson, Froschauer, Sharma, in preparation), this implicated it as a structural motor component. We inspected the peripheral part of the medial disk adjacent to $PflC_{4N}$ which disappeared when we deleted *pflD*, and found that a model of PflD fitted well into this density (Fig 2A,D).

## *The proximal disk is composed of PflA spokes and a rim of PflB*

We finally modelled the proximal disk, known to contain PflA and PflB, together with stator complex protein MotB (9). Extensive short α-helical bundles were consistent with repetitive TPR motifs, short 34-residue repeats of two antiparallel α-helices (28,29), seen in proximal disk components PflA and PflB. We modelled monomeric PflA and PflB and a PflA and PflB dimer. PflA forms an elongated superhelix consisting of 16 TPR motifs connected by an unstructured linker to an N-terminal β-sandwich domain. The structure of PflB is α-helical except for two five-residue β-sheets. These models fitted clearly into our map, with 17 radial spokes of PflA positioning a continuous rim of 17 PflBs (Fig. 2G). The PflA linker binds a TPR-superhelical groove in PflB to create a PflAB heterodimer, with the α-helical part of PflA pointing inwards, and the β-sandwich domain wrapping around PflB. To test our PflAB dimer model we measured their interaction using mass photometry. PflAB heterodimerise even at nanomolar concentrations, and deleting the putative β-sandwich interaction domain of PflA (residues 16-168) to form $PflA_{\Delta 168}$ abolished dimer formation (Fig. 2I, Fig. S6). A subtomogram average structure of the motor in a $PflA_{\Delta 168}$ mutant further confirmed that PflB is unable to assemble into the motor (Figure 2H), although the C-terminal end of PflA remains evident relative to a *pflB* deletion mutant (9) (Figure 2H). Taken together with the interaction of PflA and PflB seen in pulldowns (30), we conclude that PflAB dimerisation is essential for proximal disk assembly.

Our positioning of PflA explains two additional short densities protruding from the midpoint of each PflA superhelix. PflA is a glycoprotein, with N-linked glycans attached at asparagines 458 and 497 (31). These residues are situated at the base of these rodlike densities, meaning glycans are the best explanation for their identity (Fig. 2G, red atoms). We also saw similar protrusions from every copy of $PflC_N$ at asparagine 239 (Figure S4B), meaning PflC is also a likely glycoprotein.

We could not assign proteins to three remaining densities in the scaffold: the so-called E-ring that spaces the MS-ring from PflA, a cage previously observed in *H. pylori* (32) on the periphery of the PflB rim that extends through the membrane to wrap around the stator complexes, and a small density adjacent to PflD (Fig 2B, opaque regions). The relatively low resolution of these regions lead to many equally plausible fits of candidate proteins.

## *The periplasmic scaffold positions 17 stator complexes*

To better understand the flagellar torque-generation machinery we performed focussed refinement of the stator complexes and the outer edge of the periplasmic scaffold, enabling us to resolve the pentameric structure of MotA contacting the C-ring (Fig. 3A). We located the periplasmic peptidoglycan-binding domain of MotB by cross-referencing our previous work (9), and we were able to discern the MotB linker extending toward the membrane from the periplasmic domain. We fitted the structure of *C. jejuni* MotA into the pentameric density (33) (Fig. 3B) and a dimer of a model of the periplasmic region of MotB into the periplasmic density. Additional densities reach from the cytoplasmic face of MotA around its outer rim to contact the membrane at the same radius as the periplasmic cage. These cytoplasmic densities may be composed of proteins implicated in *C. jejuni* motility and form a structure continuous with the periplasmic scaffold (30).

An arc of density partially encircling the periplasmic MotB linker had similar radius and location as complete circles of FliL in the *H. pylori* and *Borrelia burgdorferi* motors (32,34). We found that a curved tetrameric homology model of FliL fitted well into this arc (Figure 3C). Co-immunoprecipitation assays revealed that FliL is found in pulldowns of PflA and PflB (Tables S1). Together this suggests that a partial circle of FliL is augmented by PflB and PflA to scaffold MotB (Fig. S7) and explains why PflA and PflB are both required for the high occupancy or static anchoring of stator complexes into the *C. jejuni* motor (9). Indeed, we found that deletion of *fliL* in *C. jejuni* has only a modest impact upon motility (Fig. S8) in contrast to *H. pylori* where FliL is essential.

The presence of the stator complexes in the *C. jejuni* structure, in contrast to their absence in *Salmonella,* indicates either high occupancy or static anchoring mediated by the interactions between the stators and the PflA, PflB, FliL, and potential cytoplasmic proteins. The consistent rotational register of the stator complexes in our averaged structure, with a pentameric corner pointing toward the C-ring, indicates that stator complexes are more frequently in this rotational register than any other.Conserved rotor components have adapted to a high torque role

We wondered how the *C. jejuni* rotor (the C-ring, MS-ring, and rod) has adapted to retain its function yet interact with the substantially wider stator complex ring. The *C. jejuni* C-ring is substantially wider, with a radius of 26.5 nm compared to the 21.5 nm-radius *Salmonella* C-ring. This is likely achieved by increasing the number of subunits that make up the C-ring, and based on the ratios of circumferences of the *C. jejuni* C-ring compared to the 34 copies of FliG in *Salmonella*, we estimate 42 copies of FliG in the membrane-proximal ring of the *C. jejuni* C-ring.

The *C. jejuni* MS-ring is also wider than that of *Salmonella*, consistent with the 1:1 stoichiometry of FliF to FliG (35,36). We modelled MS-rings with various FliF stoichiometries while maintaining the same inter-protomer azimuthal spacing as in *Salmonella,* whose MS-ring features 34 copies of FliF. A 42-protomer model best agreed with our observed density, and matches our C-ring estimate. We modelled the RBM1 and RBM2 domains as in previous work (37), although we found that the circumference of the inner RBM12 domains, unlike other parts of the MS-ring, was the same as in *Salmonella*. We therefore modelled 23 protomers into the inner ring as in *Salmonella*, and the outer ring the remaining 19 protomers (Fig. 3E).

We docked a homology model of the rod and export gate complex ($FlhB_N$, FliP, FliQ, and FliR at the rod tip) into our density map based on *Salmonella* structures (Fig. 3E). The model was positioned taking into account known interactions between FliF's RBM2 loop and FliP/FliQ (14). In *Salmonella*, the rod and MS-ring are intricately stitched together by multiple interactions. Rod interaction with this wider MS-ring is achieved by FlgC and FlgF sequence insertions to produce a wider rod. In contrast, the RBM2 ring in the MS-ring retains contact with FliP and FliQ in the export gate by retaining the same radial placement as in isolated *Salmonella* motors, despite change in overall FliF stoichiometry.

### *An in situ model of the type III secretion system*

The mechanism of type III secretion, key to flagellar assembly, has been elusive due to our inability to determine the structure of the N-terminal integral membrane domain of FlhA. By combining our map with structural predictions and information from previous studies we were able to place $FlhA_N$ in our model. We modelled a trimer of $FlhA_N$ with no *a priori* information about its full oligomeric state. Our trimer formed an arc with 40° inter-protomer curvature; extrapolation of this trimer yielded a complete ring that matched the established nine-protomer stoichiometry (Fig. 4A). The 6 nm-diameter cytoplasmic FHIPEP portal subdomain features a 1.7 nm channel pointing toward $FlhA_C$ and the cytoplasm. The inner and outer faces of the main $FlhA_N$ ring are hydrophobic, but while the outer face is perpendicular to the membrane, the inner face is angled at 60° to the membrane, echoing the hydrophobicity and 60° slope of the conical tip of the peri-membrane export gate (Fig. 4B). Positioning $FlhA_N$ using the relationship of this band to the membrane, visualization of the protruding cytoplasmic subdomain, and established location of $FlhA_C$ all indicated that $FlhA_N$ is spaced beneath the export gate. Indeed, the 60°-slanted faces of both $FlhA_N$ and the export gate are positively charged (Fig. 4C,D), consistent with interactions with anionic phospholipids and inconsistent with protein interfaces. Further consistent with a lack of interaction between $FlhA_N$ and the export gate, attempts to dock the $FlhBFliQ_4$ export gate tip into the $FlhA_N$ nonamer failed using AlphaFold2 (38,39), MDockPP (40), and GRAMM (41). We suggest the best way to reconcile these observations is that a truncated cone of phospholipids separates $FlhA_N$ from the export gate. Nevertheless, the axial atrium between the export gate and $FlhA_N$ cannot accommodate $FlhB_C$. Modelling $FlhB_C$ and its linker from $FlhB_N$ onto the tip of our export gate homology model suggests that $FlhB_C$ reaches through the $FlhA_N$ nonamer toward $FlhA_C$.

# Discussion

We determined a near-complete molecular model of the bacterial flagellar motor from C. jejuni using in situ electron cryomicroscopy imaging, an important step in understanding motor function and our long term goal of understanding the evolution of a complex molecular machine. Our approach is a proof-of-principle demonstration of the power of using minicells and single particle analysis for high-resolution of motors, and extends imaging procedures used for abundant surface-exposed structures to scarce structures embedded in the cell. Our results, including a structure to sufficient resolution for molecular model docking and refinement, provide a near-complete inventory of the proteins incorporated into the

Campylobacterota motor during evolution of higher torque output and the adaptations of pre-existing components (Table S2). Our results also provide insights into universal principles of flagellar rotation and type III secretion.

The architecture of the basal disk suggests its evolutionary origin. FlgP is the major component of the basal disk, with 17 FlgP trimeric repeats that may dictate the symmetry of the remainder of the periplasmic scaffold. FlgP is a member of lipoprotein InterPro family IPR024952, which also includes *Helicobacter* Lpp20. A key difference is that the SHS2 domain of FlgP is modified by a β-hairpin insertion between the α-helix and second β-sheet. This insert is also evident in FlgT, which also forms outer membrane-associated rings in γ-proteobacterial flagellar motors (42). FlgP-like proteins evidently have longstanding associations with flagellar motors for building outer-membrane associated structures, and formation of rings perhaps facilitated by a β-hairpin oligomerisation insert. Curiously, the basal disk from *Wolinella* has been proposed to form a spiral, not concentric rings (43). Concentric rings best explain the uniform and well-resolved PflC densities around the *C. jejuni* motor and a snug fit of the basal disk around the P-ring that templates the remaining 17-fold symmetry. *Wolinella* lacks a PflC lattice (10) raising the possibility that FlgP forms archimedean spirals only in the absence of PflC.

Similarly, the architecture of the medial disk suggests its origin. The medial disk is made of a lattice of PflC, a protein with the domain organisation and structure of HtrA-family enzymes, although lacking the catalytic residues (Fig S4C) (44). The innermost $PflC_1$ ring forms a daisychain of 17 protomers composed of the N-terminal domain from one polypeptide and the C-terminal domain from another, a protomer that superimposes on monomeric HtrA. This inner ring adapts the 51-fold symmetry of the innermost FlgP ring to the 17-fold symmetry of the periplasmic scaffold, and a lattice of six additional PflC protomers, $PflC_{2-7}$, assemble on each inner $PflC_1$, resulting in a lattice of 119 PflC chains. HtrA also forms higher-order oligomers (25), suggesting that this oligomerisation tendency may have been present for exaptation to function as a structural scaffold. HtrA family proteins are secreted to the periplasm, meaning that they already co-localised to the same subcellular locale as the flagellar motor. Taken together, the similarities in domain organisation suggest PflC is descended from an ancient HtrA protease. PflC sequences in *Wolinella* and *Helicobacter* species motors that lack a medial disk do not have the inter-PDZ domain linker that mediates the head-to-tail oligomerisation of the PflC ring between the basal disk and PflAB.

The ancestry of PflA and PflB, which comprise the proximal disk, is less clear, due to the ubiquity of TPR motifs. TPR motifs are widespread building blocks of structural scaffolds; for example, the Tol/Pal component YbgF features TPR motifs (45). Parts of the Tol/Pal system

share homology with flagellar components, consistent with recruitment of a colocalised and abundant structure (6), but little more can be said at this stage.

As well as the identity and possible origins of the novel structures in the *C. jejuni* flagellar motor, our structure reveals adaptations of core components necessary in the evolution of higher torque. Three major changes are evident in the rotor components to mediate adaptation of the conserved core to the additional stator complexes. First, the radius of the MS-ring has increased to template a wider C-ring to maintain contact with the larger stator ring by increasing the stoichiometry of FliF from 34 to 42. Second, the rod needs to retain contact with this wider MS-ring, achieved by sequence insertions in FlgC, and to a lesser extent FlgF to pad the space introduced by a wider rod. It will be intriguing to probe whether rod diameter is solely responsible for increased MS-ring symmetry. Third, the RBM2 ring of the MS-ring retains the symmetry it has in *Salmonella.* FliF has previously been proposed to be a symmetry adapter, and this is further evidenced here, with RBM2 retaining the same architecture as in *Salmonella* while other parts acquire higher symmetries.

Stator components have also evolved in *C. jejuni*. The stator complexes are enclosed by a cage of PflA, PflB, FliL, and as-yet-unidentified proteins. MotB interacts with this structure, required for the high occupancy or static positioning of the *C. jejuni* stator complexes (9). It is unclear whether *C. jejuni* MotB also still interacts with peptidoglycan. The putative peptidoglycan binding site of MotB is exposed but angled towards the flagellar axis. In *E. coli*, peptidoglycan is located 20 nm above the inner membrane (46), beyond the reach of MotB's periplasmic domain in *C. jejuni.* MotB may indirectly bind peptidoglycan that is clamped by the motor's proteinaceous lattice. Indeed, purified *C. jejuni* peptidoglycan have 50 nm-wide polar holes (47), suggesting that peptidoglycan extends into the ~80 nm-wide protein lattice.

These results enhance our understanding of how high torque evolved in the Campylobacterota. A wider C-ring may have initially only required insertions into the proximal rod, leading to wider MS- and C-rings. The width of the stator complex ring does not need to rigidly track with C-ring width (9), and subsequent addition of the periplasmic scaffold could add a larger ring of additional stator complexes, a process involving recruitment of FlgP and PflC from members of the Lpp20 and HtrA family, respectively, among others. Our pseudoatomic model of structures unique to Campylobacterota and their interfacing with core flagellar components, combined with phylogenetic analysis will enable further studies to probe how novel interfaces arose during protein recruitment. Our next steps will be to determine phylogenies of these new components, clarify and experimentally validate binding interfaces, and work toward ancestral sequence reconstructions to test

hypotheses as to how novel protein interfaces emerge, and how components become essential. PflC is particularly promising given the absence of the PflC-composed medial disk in other Campylobacterota.

Our study also sheds light on universal flagellar mechanisms. We were surprised to find that our resolution was sufficient to discern the pentameric shape of MotA. This indicates a consistent rotational register of the MotA pentamer, in which the vertex of pentamers is closest to the C-ring. We attempted focused classification of individual stator complexes but failed to resolve classes with other rotational registers. Given the symmetry mismatch between the 17 stator complexes and 42 FliG protomers, we would expect that a high duty ratio of the stator complexes would result in a continuum of rotational registers and therefore an averaged structure of a homogenous circle instead of a pentamer. Predictions of stator complexes having a high duty ratio assumed an elastic linker from peptidoglycan to MotA as in *Salmonella* (48), although this does not hold for *C. jejuni* in which stator complexes are rigidly encased in their proteinaceous cage. Our structure is therefore consistent with recent results suggesting that the motor has a low duty ratio (49), and MotA's rotational register is dictated by an energy minimum of rotation around MotB instead of against FliG.

One longstanding mystery has been how the T3SS assembles and functions. Our structure contextualises previous studies to explain why $FlhA_N$ has been recalcitrant to structure determination. We believe that the structure of $FlhA_N$ has not been determined because while $FlhA_N$ domains remain monomeric until in a conical membrane, which is imposed by the export gate; detergents no longer provide this context. This explains why FliPQR assemble without FlhA and pucker the membrane (50), the absence of co-evolutionary signal between FlhA and export gate components (51), and the complex-confounding symmetry mismatch between the asymmetric export gate and FlhA. The export gate must therefore assemble first (20). $FlhA_C$ nonamers independently oligomerise tethered to nine monomeric $FlhA_N$ transmembrane domains ($FlhA_C$ oligomerization is a prerequisite for formation of a membrane dome likely to be $FlhA_N$ (52)). The intrinsic curvature of $FlhA_N$ transmembrane interfaces attract them to the membrane cone imposed by the export gate where they oligomerise around the export gate and FlhB linker, leaving $FlhB_C$ on the membrane-side of $FlhA_N$ and $FlhB_N$ on the cytoplasmic side (indeed, FlhA assembly needs the export gate but not the cytoplasmic $FlhB_C$ domain (52)). Thus while the export gate mediates $FlhA_N$ oligomerisation, it does so indirectly.

The separation and high-order symmetry mismatch of $FlhA_N$ from the export gate hints that FlhA can rotate relative to the export gate. The opposed positive charges between the $FlhA_N$ and the export gate may function like a 'Maglev' to keep the two components separate in

combination with a ring of phospholipids (Fig. 4E). The export gate is contiguous with the cytoplasmic ATPase, FliI (through FliF and the C-ring), indicating that FliI is static relative to the export gate. FliJ, however, which may rotate in the axial channel through FliI, contacts FlhA. We propose that ATP hydrolysis by FliI powers rotation of FliJ and FlhA relative to the other rotor components. The bacterial flagellar motor thus has three distinct rotating subcomplexes: the static stator structure including the periplasmic scaffold and LP-rings; the rotor including the C-ring, MS-ring, rod, and majority of the T3SS, and FlhA and FliJ.

The principal limitation of our approach is our reliance on the prominent 17-fold symmetry of the periplasmic scaffold and stator complexes. In the case of *C. jejuni* flagellar components with other symmetries, prior knowledge of the symmetry of conserved components in *Salmonella* enabled us to overcome these limitations. And while our resolution is insufficient to resolve residue-level interactions, it is sufficient to unambiguously assign domains to densities. Nevertheless, two insights lie beyond our reach. This first is how consecutive rings of FlgP in the basal disk interface to construct a rigid structure that can bend the membrane despite inherent inter-ring symmetry mismatch. The second is how the E-ring, which appears to contain densities interfacing with PflA and PflC (i.e., stator components) interacts with the MS-ring (i.e., a rotor component). The inner radius of the E-ring does not share the 17-fold symmetry of the periplasmic scaffold, and the implications of this will remain unclear until it can be determined.

Our study is the first to achieve sufficient resolution to build molecular models of a bacterial molecular machine *in situ*, providing invaluable information on the mechanisms of torque generation and secretion and enabling us to advance our understanding of the evolutionary origins of bacterial flagellar motors and providing invaluable information on the mechanisms of torque generation and secretion. Our approach confirms that using single particle analysis of protein machines *in situ* can provide sufficient resolution for molecular modelling. We posit that *in situ* imaging in the future will increasingly involve optimised cellular systems such as the one described here to provide high resolution projection images that can be mapped onto low-resolution density envelopes derived from subtomogram averaging datasets. The future of structural biology is *in situ*.

# Acknowledgements

We thank Paul Simpson in the Imperial College London Electron Microscopy Centre and the Francis Crick Institute Structural Biology science technology platform for electron microscopy assistance, and Willie Taylor for initial thoughts on modelling the transmembrane region of

FlhA. This work was supported by Medical Research Council grant MR/V000799/1 to EJC and MB, Human Frontier Science Program grant RGP0028/2021-HOCHBERG to MB and GH, NIH grant R01AI065539 to DRH, BBSRC doctoral training grant BB/M011178/1 and a short-term DAAD grant to TD. PBR is supported by the Francis Crick Institute, which receives its core funding from Cancer Research UK (CC2106), the UK Medical Research Council (CC2106), and the Wellcome Trust (CC2106). CMS is supported by research grants Sh580/7-2 and Sh580/8-2 in the framework of the DFG (Deutsche Forschungsgemeinschaft) priority program SPP2002 (Small proteins in prokaryotes, an unexplored world), the DFG Research Training Group GRK2157 “3D-Infect”, and a “CampyRNA” junior consortium grant within the 2nd call of Infect-ERA (ERA-NET; www.infect-era.eu)/Bundesministerium für Bildung und Forschung (BMBF; www.bmbf.de).



# Author Contributions

TD: sample prep, image processing, analysis, molecular modelling, mass photometry, wrote paper, EJC: sample prep, image processing, analysis, NS: image processing, TU: sample prep, data acquisition, image processing, AN: data acquisition, image processing, DR: flgQ-mCherry, pulldowns, fliL knockout, SS, KF, MA, CS: PflC and PflD identification, LDH: PflD subtomogram averaging, GH, SGG: Mass photometry data acquisition supervision and analysis, funding acquisition, DRH: flgQ-mCherry, pulldowns, funding acquisition, PR: image processing, funding acquisition, MB: conceptualization, funding acquisition, supervision, wrote paper

# Declaration of Interests

The authors declare no competing interests.

# Figure titles and legends

**Figure 1. Engineering of homogenous *Campylobacter jejuni* minicells enabled us to determine the *in situ* structure of a flagellar motor by single particle analysis electron cryo-microscopy (A) Schematic of the flagellar motor from *C. jejuni.* Proton flux through the stator complexes drives rotation of the C-ring, MS-ring, rod, and hook/filament. In the Campylobacterota, a basal disk and periplasmic scaffold have evolved that scaffold a wider ring of additional stator complexes thought to be increase motor torque. IM/OM: inner/outer membrane (B) WT *C. jejuni* cells typically provide 1 flagellar motor per field of view as compared to (C) many motors per field of view in our minicells strain, greatly increasing throughput (D) Periplasmic and cytoplasmic features are evident in 2-D classes of manually picked motors. (E) Cross-section through an isosurface rendering of a whole-motor 3-D reconstruction. (F) Density map from (E), segmented and exploded along the z-axis to highlight component structures.**

**Figure 2. An enlarged ring of 17 stator complexes are held in place by a periplasmic scaffold composed of novel proteins. (A) Whole-motor map shows that the scaffold attaches to the innermost ring of the basal disk, which itself is a series of concentric rings. Different sections of the periplasmic scaffold and basal disk in colour. (B) Docked and refined molecular models of the scaffold and basal disk, in a transparent density map. Regions unaccounted-for by molecular models are shown as solid. Shown is an asymmetric unit of the C17-symmetric structure in side view. (C) The refined scaffold map and basal disk density (right) and fitted structural models (left) of known basal disk and scaffold proteins. The models have been exploded along the horizontal axis. (D) *pflC* and *pflD* deletion leads to discrete losses in subtomogram average structures of resultant motors (magenta boxes depict losses). (E) Structure of the basal and medial disks, showing docked and refined FlgP (purple), PflC (the inner most ring, $PflC_1$, magenta; spokes of six additional monomers per asymmetric unit, $PflC_{2\text{-}7}$, teal), and PflD (black) models. Right panel: Each FlgP contacts the next two subunits by an extended β-sheet, interlocking to form rings. The innermost ring has 51 FlgPs, to which are attached 17 copies of the innermost ring of PflC, i.e., $PflC_1$ (magenta). $PflC_{1C}$ domains interact with every third FlgP and contact $PflC_{1N}$ of the next monomer in a head-tail fashion. A single PflC molecule contributes to two protomers (magenta outline) (F) Left: The medial disk is a protein lattice of an additional six PflC chains per asymmetric unit of the 17-fold symmetric periplasmic structure. These $PflC_{2\text{-}7N}$ domains (teal) have a different arrangement to the inner FlgP-binding $PflC_1$s. Right: PflD (black) is attached to the $PflC_{4N}$ on the edge of the $PflC_{2\text{-}7}$ lattice, and forms part of a bridge that connects the medial and proximal disks. Isosurface threshold increased to demonstrate fit to map. (G) Top view of an asymmetric unit of the proximal disk. PflA (light green) is positioned radially like spokes, interacting at its N-terminal end with PflB (dark green) at the outer edge of the scaffold. An arc of FliL (red) and periplasmic domain of MotB (pink, residues 68-247) are also accounted for. (H) Deleting the β-sandwich and linker of PflA prevents incorporation of PflB into the motor. (I) Mass photometry measurements confirm the PflAB dimer (red background) forms *in vitro*. Deleting the β-sandwich and linker domains of PflA abolishes dimer formation. (J) FlgP shares the SHS2-like fold with Lpp20 of *Helicobacter pylori* and FlgT of *Vibrio alginolyticus*. All are OM-associated and FlgT is a flagellar component, indicating shared evolutionary origin. (K) A domain-swapped PflC shares its domain architecture and overall fold with HtrA, a serine protease.**

**Figure 3. Wider rings of additional stator complexes are incorporated in the scaffold while the rotor components are correspondingly wider. (A) A focused refinement of the stator complexes reveals 17 pentameric densities on the cytoplasmic face of the IM. (B) A structure of transmembrane MotAB (PDB ID 6ykm) fitted into the pentameric stator density in our whole-motor map. There are additional unaccounted densities on the cytoplasmic side of MotA. (C) A tetrameric arc of FliL wraps around the MotB stalk. (D) Flagellar motor of *Salmonella* does not contain any periplasmic scaffolding structures. Models of the LP-rings, rod and FliF (14) are docked into a STA structure of an *in situ Salmonella* motor (9). (E) The rotor (rod, MS-ring, and C-ring) of *C. jejuni* is wider than that of *Salmonella*. Insertions in FlgF and FlgC in *C. jejuni* retain contact with the MS-ring. The MotAB stator is embedded in the inner membrane and periplasmic scaffold. The Periplasmic domains of MotB form an apparent complex with PflA, PflB, and FliL.**

**Figure 4. A model of the flagellar type III secretion system suggests that FlhA is separated from the export gate by a band of phospholipds. (A) Hydrophobicity of $FlhA_N$ depicting reveals hydrophobic bands on the outer and inner rims of the $FlhA_N$ nonamer. The inner band is angled at 60° to the plane of the membrane. (B) Hydrophobicity of the export gate reveals a matching hydrophobic band. (C) Electrostatic potential reveals a positively charged band at the base of the $FlhA_N$ funnel, corresponding to (D) a positively charged region around the neck of the FlhB linker. (E) A model for the structure of the flagellar type III secretion system in situ suggests that FlhA and the export gate are discrete structures that might be capable of rotating relative to one-another.**

# Tables with titles and legends

**Table 1: List of bacterial strains and plasmids used in this work.**

| Description/ name | Bacterial strain or plasmid | Source |
|---|---|---|
| *C. jejuni* DRH212 | *C. jejuni* 81-176 *rpsl*$^{Sm}$ ($Sm^R$) | (53) |
| *C. jejuni* Minicell-producing strain | *C. jejuni* 81-176 Δ*flhG* Δ*flaAB* | This work |
| *C. jejuni* PflA truncation | *C. jejuni* 81-176 $pflA_{\Delta 18\text{-}168}$ | This work |
| *C. jejuni* NCTC11168 WT CSS-0032 | *C. jejuni* NCTC11168 wildtype | This work |

| | | |
|---|---|---|
| *C. jejuni* PflC deletion CSS-4087 | *C. jejuni* NCTC11168 △*cj1643* | This work |
| *C. jejuni* PflD deletion CSS-4081 | *C. jejuni* NCTC11168 △*cj0892c* | This work |
| *C. jejuni* PflC-3xFLAG CSS-4720 | *C. jejuni* NCTC11168 Cj1643-3xFLAG | This work |
| *C. jejuni* PflD-sfGFP CSS-4666 | *C. jejuni* NCTC11168 △*cj0892c* + *cj0892c-sfgfp* | This work |
| *C. jejuni* PflD-sfGFP, PflA-3xFLAG CSS-5714 | *C. jejuni* NCTC11168 △*cj0892c* + *cj0892c-sfgfp*, PflA-3xFLAG | This work |
| *C. jejuni* PflD-sfGFP, PflB-3xFLAG CSS-5716 | *C. jejuni* NCTC11168 △*cj0892c* + *cj0892c-sfgfp*, PflB-3xFLAG | This work |
| pRY109 | source of *cat* cassette for chloramphenicol resistance reference: | DOI: 10.1016/0378-1119(93)90355-7 |
| pRY112 | *E. coli-C. jejuni* shuttle vector | DOI: 10.1016/0378-1119(93)90355-7 |
| pDAR1003 | pRY112 with 76-bp fragment containing *cat* promoter with start codon and in- frame BamHI restriction site cloned into the XbaI and XmaI sites | This work |
| pDAR1006 | pDAR1003 with DNA encoding *mcherry* and stop codon cloned in-frame with respect to the *cat* start codon and BamHI site into the XmaI and EcoRV sites | This work |
| FlgQ-mCherry plasmid pDRH7476 | with *flgQ* from codon 2 to the penultimate codon cloned into the BamHI site of pDAR1006 to create a FlgQ-mCherry fusion | This work |
| *C. jejuni* FlgQ-mCherry DRH7516 | *C. jejuni* 81-176 △*flgQ* / *pDRH7476* | This work |
| Cloning strain | *E. coli* DH5α | Lab stock |
| Protein expression strain | *E. coli* BL21(DE3) | Lab stock |
| Cloning vector backbone | pLIC ($Amp^R$) | Franziska Sendker |
| Full-length PflA (16-788) | pLIC-PflA | This work |

| | | |
|---|---|---|
| PflA TPR regions (169-788) | pLIC-PflAα | This work |
| PflA N-terminal half (16-454) | pLIC-PflA$_N$ | This work |
| Soluble PflB (113-820) | pLIC-PflB | This work |
| Full-length PflC (17-364) | pLIC-PflC | This work |
| PflC C-terminal truncation (17-235) | pLIC-PflC$_{\triangle 236\text{-}349}$ | This work |
| *C. jejuni* DAR1124 | C. jejuni 81-176 *rpsL*$^{Sm}$ *ΔpflA* | (9) |
| *C. jejuni* DAR3447 | C. jejuni 81-176 *rpsL*$^{Sm}$ *ΔpflA/pDAR3417* | This work |
| *C. jejuni* DAR3477 | C. jejuni 81-176 *rpsL*$^{Sm}$ *ΔpflA/pDAR1604* | This work |
| *C. jejuni* DAR981 | C. jejuni 81-176 *rpsL*$^{Sm}$ *ΔpflB* | (9) |
| *C. jejuni* DAR3451 | C. jejuni 81-176 *rpsL*$^{Sm}$ *ΔpflB/pDAR3414* | This work |
| *C. jejuni* DAR3479 | C. jejuni 81-176 *rpsL*$^{Sm}$ *ΔpflB/pDAR965* | This work |
| pRY108 | *E. coli-C. jejuni* shuttle vector | (54) |
| pECO102 | *E. coli-C. jejuni* shuttle vector containing cat promoter and start codon for expression of genes for complementation | (55) |
| pDAR965 | *E. coli-C. jejuni* shuttle vector containing cat promoter and start codon followed by DNA encoding an in-frame N-terminal FLAG tag | (56) |
| pDAR1425 | pRY108 with 206 base pair fragment containing flaA promoter and start codonwith in-frame SpeI site cloned into the XbaI and BamHI sites | This work |
| pDAR1604 | E. coli-C. jejuni shuttle vector containing flaA promoter and start codon followed by DNA encoding an in-frame N-terminal FLAG tag | (57) |
| pDAR3414 | pECO102 with codon 2 to penultimate codon of pflB and an in-frame C- | This work |

| | | |
|---|---|---|
| | terminal FLAG epitope cloned into the BamHI site | |
| pDAR3417 | pDAR1425 with codon 2 to penultimate codon of pflA and an in-frame C-terminal FLAG epitope cloned into the BamHI site | This work |

570 **Table 2: Data collection statistics of two cryoEM data collection sessions.**

| Parameter | Dataset 1 (“F3”) | Dataset 2 (“K2”) |
|---|---|---|
| Voltage (kV) | 300 | 300 |
| Detector | Falcon III | K2 |
| Pixel size (Å/px) | 1.75 | 2.2 |
| Exposure dose per frame ($e^-$/Å/frame) | 5 | 1.53 |
| Total exposure dose ($e^-$/Å) | 50 | 50 |
| Defocus range (μm) | -1.5 to -3.0 | -1.5 to -3.0 |
| Total micrographs | 8,774 | 42,988 |

571

# 572 Methods

## 573 *Resource availability*

### 574 Lead contact

575 Further information and requests for resources and reagents should be directed to and will
576 be fulfilled by the lead contact, Morgan Beeby (mbeeby@imperial.ac.uk)

### 577 Materials availability

578 Plasmids and strains generated in this study are available on request from the lead author.

### 579 Data and code availability

### 580 Data resources

581 The cryo-EM map of the whole-motor map has been deposited in the Electron Microscopy
582 Data Bank (EMDB) with accession code EMD-16723 together with the original micrographs
583 deposited to the EMPIAR repository with public accession code EMPIAR-11580 (DOI:

584 10.6019/EMPIAR-10016). The refined periplasmic scaffold map has been deposited in the
585 EMDB with accession code EMD-16724. STA maps have been deposited in the EMDB with
586 the following accession codes: Δ*pflC* - EMD-17415; Δ*pflD* - EMD-17416; *pflA*$_{\Delta 16\text{-}168}$ - EMD-
587 17417, FlgQ-mCherry - EMD-17419.

588 **Experimental model and study participant details**

589 Please see Table 1 for details of strains and plasmids used in this study.

590 ## *Method details*

591 **Bacterial strains and growth conditions**

592 *C. jejuni* 81-176 or NCTC11168 were cultured from frozen stocks on Mueller-Hinton (MH)
593 agar (1.5% w/v) supplemented with trimethoprim (10 µg/mL) (MHT) for 1-2 days at 37°C
594 under microaerophilic conditions (5% O2, 10% CO2, 85% N2) in a in a Heracell 150i trigas
595 incubator (Thermo Fisher Scientific). Additional antibiotics were added to the agar medium
596 when required: kanamycin (Km) at 50 µg/mL, streptomycin (Sm) at 2 mg/mL. All 81-176
597 mutants were constructed in DRH212 (53), a streptomycin resistant derivative of *C. jejuni*
598 81-176, which is the reference wild-type strain in this work unless otherwise stated. All
599 constructed strains are listed in Table 1.

600 When working with *E. coli*, cultures were grown at 37°C on Luria-Bertani (LB) agar plates
601 (1.5% w/v) or in LB medium with agitation, both supplemented with carbenicillin at 100
602 µg/ml.

603 **Strain construction**

604 The minicell (*⍙flhG ⍙flaAB*) and PflA truncation (*pflA*$_{\Delta 18\text{-}168}$) strains were constructed as
605 described previously (53,58). Briefly, *aphA-rpsL*$^{WT}$ cassettes flanked by ~500 bp overhangs
606 with homology to the targeted chromosomal loci and ecoRI sites at the 5' and 3' termini were
607 synthesised by "splicing by overlap extension" PCR (SOE PCR). Linear DNA fragments
608 were methylated at their ecoRI sites with ecoRI methyltransferase (New England Biolabs)
609 and transformed into *C. jejuni* using the biphasic method (59). Transformants were selected
610 for on MH agar supplemented with 50 µg/mL kanamycin. Replacement of the *aphA-rpsL*$^{WT}$
611 with the desired mutation was achieved using the same method, but with transformants
612 being selected for on MH agar supplemented with 2 mg/mL streptomycin sulfate.
613 Kanamycin-sensitive, streptomycin-resistant transformants were single-colony purified and
614 checked by Sanger sequencing (Source Biosciences UK). For the minicell background, in-

615 frame deletion of *flhG* leaves the first and last 20 codons intact, while the Δ*flaAB* allele spans
616 from 20 base pairs upstream of the *flaA* translational start site to codon 548 of *flaB.*

617 To construct the *C. jejuni fliL* mutant, we made a *cat* insertional knockout and confirmed
618 absence of polar effects. To preserve expression of the essential *acpS* gene downstream of
619 fliL, we constructed a *fliL* mutant that disrupted *fliL* with an antibiotic-resistance cassette
620 containing an intact flaA promoter positioned to maintain expression of acpS. First, the *fliL*
621 locus from *C. jejuni* 81-176 was PCR amplified with a HpaI site engineered within the *fliL*
622 coding sequence. This fragment was then cloned into the BamHI site of pUC19 to create
623 pDAR1712. The flaA promoter and start codon were PCR amplified from *C. jejuni* 81-176
624 and cloned into the XbaI and BamHI sites of pUC19 to create pDAR2039. The
625 chloramphenicol-resistance cassette containing cat was digested as a PstI fragment from
626 pRY109 and cloned into PstI-digested pDAR2039 to create pDAR2045. The *cat-flaA*
627 promoter was then digested from pDAR2045 as a EcoRI-BamHI fragment, treated with T4
628 DNA polymerase to create blunt ends and cloned into the HpaI site of pDAR1712 to create
629 pDAR2072. pDAR2072 was verified to contain the *cat-flaA* promoter in the correct
630 orientation to maintain expression of *acpS*. DRH212 was then electroporated with
631 pDAR2072 and chloramphenicol-resistance transformants were recovered. Colony PCR
632 verified creation of a *fliL* mutant (DAR2076).

633 Deletion mutants of *C. jejuni* NCTC11168 were constructed by double-crossover
634 homologous recombination with an antibiotic resistance cassette to remove most of the
635 coding sequence using overlap PCR products. As an example, deletion of *cj1643* (*pflC*) is
636 described. First, ~500 bp upstream of the *cj1643* start codon was amplified using CSO-
637 3359/3360 and ~500 bp downstream of the *cj1643* stop codon was amplified with CSO-
638 3361/-3362 from genomic DNA (gDNA) of the wild-type strain (CSS-0032). A non-polar
639 kanamycin resistance cassette (*aphA-3*, $Kan^R$) (Skouloubris et al., 1998) was amplified from
640 pGG1 (60) with primers HPK1/HPK2. To fuse the up- and downstream regions of *cj1643*
641 with the resistance cassette, the three fragments were mixed and subjected to overlap-
642 extension PCR with CSO-3359/ 3362. PCR products were electroporated into the WT strain
643 as previously described (61). The final deletion strain (CSS-4087; NCTC11168 Δ*cj1643*) was
644 verified by colony PCR with CSO-3363/HPK2. Deletion of *cj0892c* (*pflD*) in *C. jejuni* strain
645 NCTC11168 was generated in a similar fashion: *cj0892c*::*aphA-3* (CSS-4081; NCTC11168
646 Δ*cj0892c*).

To fuse *sfgfp* fusion to the penultimate codon of *cj0892c* (*pflD*), its coding sequence was first amplified with CSO-3611/3612, digested with *Nse*I/*Cla*I, and inserted into similarly-digested pSE59.1 ((62); amplified with CSO-0347/CSO-0760) to generate pSSv106.5, where *cj0892c* transcription is driven from the *metK* promoter. The plasmid was verified by colony PCR with CSO-0644/3270 and sequencing with CSO-0759. Next, *sfgfp* was amplified from its second codon from pXG10-SF (63) with CSO-3279/3717, digested with *Cla*I, and ligated to pSSv106.5 (amplified with CSO-3766/0347 and also digested with *Cla*I). This generated pSSv114.1, which was verified by colony PCR with CSO-0644/0593 and sequencing with CSO-0759/3270. The fusion of *rdxA*::$P_{metK}$-*cj0892c*-sfGFP was amplified from pSSv114.1 with CSO-2276/2277 and introduced into the *rdxA* locus of △*cj0892c* (CSS-4081) by electroporation. Clones were verified via colony PCR and sequencing with CSO-0349 and CSO-0644. Colony PCR was also used to confirm retention of the original deletion with CSO-3343 and HPK2.

Similar to construction of deletion mutants, C-terminal epitope tagged strains were generated by homologous recombination at the native locus by electroporation of a DNA fragment. The 3xFLAG sequence was fused to the penultimate codon of the coding sequence to allow in-frame translation of the tag. The DNA fragment contained ~ 500 bp upstream of the penultimate codon of the gene of interest, the sequence of the epitope tag, a non-polar resistance cassette, and the ~500 bp downstream sequence of the gene. As an example, 3xFLAG tagging of PflA (CSS-5714) is described. The upstream fragment was amplified with CSO-4224 and CSO-4225 from *C. jejuni* NCTC11168 WT gDNA. The downstream fragment was amplified using CSO-4226 and CSO-4227. The fusion of the 3xFLAG tag with the gentamicin resistance cassette was amplified from *fliW*::3xFLAG-*aac*(3)-IV (60) using CSO-0065 and HPK2. Next, a three-fragment overlap PCR using CSO-4224 and CSO-4227 was performed and the resulting PCR product was electroporated into CSS-4666. The obtained clones were validated by PCR using CSO-4223 and HPK2 and by sequencing using CSO-4223. PflB-3xFLAG (CSS-5716) and PflC-3xFLAG (CSS-4720) were generated similarly. The 3xFLAG with a non-polar kanamycin resistance cassette was amplified from *csrA*::3xFLAG-*aphA*-3 (60).

To construct a FlgQ-mcherry fusion protein for expression, a 76-bp DNA fragment containing the cat promoter and start codon with an in-frame BamHI site from pRY109 was amplified by PCR and cloned into the XbaI and XmaI sites of pRY112 to create pDAR1003. PCR was then used to amplify mcherry from codon to the stop codon, which was then inserted into XmaI and EcoRV sites of pDAR1003 to create pDAR1006. This plasmid contains a start

codon that is in-frame with DNA for BamHI and XmaI sites followed by the mcherry coding sequence. Primers were then designed and used for PCR to amplify flgQ from codon 2 to the stop codon from C. jejuni 81-176. This fragment was inserted in-frame into the BamHI site of pDARH1006 to create pDRH7476, which was then conjugated into DRH2071 to result in DRH7516.

**CryoEM sample preparation**

*C. jejuni* Δ*flhG* Δ*flaAB* cells were grown on MH plates and resuspended in phosphate-buffered saline (PBS buffer, 137 mM NaCl, 2.7 mM KCl, 10 mM Na2HPO4, 1.8 mM KH2PO4, pH 7.4). Cells were spun at 4,000 rpm for 20 min to pellet whole cells. The minicell-enriched supernatant was removed and spun in a tabletop microcentrifuge at 15,000 rpm for 5 min to pellet the minicells. The pellet was then resuspended to a theoretical OD600 of ~15.

Minicells were vitrified on QUANTIFOIL® R0.6/1 or R1.2/1.3 holey carbon grids (Quantifoil Micro Tools) using a Vitrobot Mark IV (Thermo Fisher Scientific).

For cryoET, whole-cells were grown on MHT agar, re-streaked on fresh plates and grown overnight before use. Freshly grown cells were suspended into ~1.5 mL of PBS buffer and concentrated to an approximate theoretical $OD_{600}$ of 10 by pelleting at 3000 rpm for 5 min on a tabletop microcentrifuge and resuspending appropriately. 30 µL of the concentrated cell sample was mixed with 10 nm gold fiducial beads coated with bovine serum albumin (BSA). 3 µL of this mixture was applied to freshly glow-discharged QUANTIFOIL® R2/2, 300 mesh grids. Grids were plunge-frozen in liquified ethane-propane using a Vitrobot mark IV.

**Image acquisition**

Micrographs of the minicell sample were collected using a 300 keV Titan Krios TEMs (Thermo Fisher Scientific), across two sessions. The first dataset was collected on a microscope with a Falcon III direct electron detector (Thermo Fisher Scientific), the second dataset using a K2 direct electron detector equipped with a GIF energy filter (Gatan), using a slit width of 20 eV. Due to our large particle size relative to that of the holes, we collected one shot per hole. Gain correction was done on-the-fly. Details of data collection parameters are described on Table 2.

**Tilt series acquisition**

Tilt series of motors in *pflA*$_{\Delta 18\text{-}168}$ were collected using a 300 keV Titan Krios TEM (Thermo Fisher Scientific) equipped with a K2 direct electron detector and a GIF energy filter (Gatan) using a slit width of 20 eV. Data was collected in Tomography 5 (Thermo Fisher Scientific) using a dose-symmetric tilt scheme across ±57° in 3° increments. We used a dose of 3 $e^-/Å^2$ per tilt, distributed across 4 movie frames. The pixel size was 2.2 Å and defocus range from -4.0 to -5.0 µm. All other tilt series datasets were acquired on a 200-kV FEI Tecnai TF20 FEG transmission electron microscope (FEI Company) equipped with a Falcon II direct electron detector camera (FEI Company) using Gatan 914 or 626 cryo-holders. Tilt series were recorded from −57° to +57° with an increment of 3° collected defocus of approximately −4 µm using Leginon automated data-collection software at a nominal magnification of 25,000× and were binned two times. Cumulative doses of ~120 $e^-/Å^2$ were used. Overnight data collection was facilitated by the addition of a 3-L cold-trap Dewar flask and automated refilling of the Dewar cryo-holder triggered by a custom-written Leginon node interfaced with a computer controlled liquid nitrogen pump (Norhof LN2 Systems).

**Single particle analysis**

Movie frames were aligned and dose-weighted according to exposure, as implemented in MotionCor 2.1 (64). All subsequent processing was done in RELION 3.1 (65,66). CTF-correction was performed using CTFFIND4 (67), using the RELION wrapper. Flagellar motor positions were picked manually, yielding 79,287 particle coordinates for the K2 dataset and 14,605 particle coordinates in the F3 dataset.

The two datasets were first processed separately in RELION 3.1, before merging for a final round of refinement For the K2 dataset, 79287 particles were extracted at a box size of 800 px. A round of 2D classification removed junk and membrane particles, and an initial model was created using these particles with imposed C17 symmetry, which is known from past structural characterisation of the motor by subtomogram averaging (9). A round of mask-free 3D classification and refinement with applied C17 symmetry produced the first consensus refinement. 27,164 particles were then re-extracted, centering on the periplasmic structures. After another round of 3D classification, 19,736 particles were refined in C17 symmetry to produce a whole-motor reconstruction at 9.88 Å using gold-standard

refinement. For the F3 data, 14,605 particles were extracted at a box size of 1000 px rescaled to 500 px. They underwent 2D classification to remove junk, 3D classification and refinement to arrive at an initial consensus 3D structure. The particles were again re-centered on the periplasmic structures and underwent another round of refinement. Finally, the 13,054 particles were re-extracted at an un-binned 1000 px box size for a final round of refinement. The two re-centered refined datasets were merged, assigning them different RELION 3.1 optics groups, and refined to a global resolution of 9.36 Å (32,790 total particles).

Signal subtraction was used to further refine the structure of the periplasmic scaffold. A mask encompassing the regions of interest was made by segmenting and smoothing the whole-motor map using UCSF Chimera 1.16 (68,69) and its Segger plugin (70), binarising and adding a soft-edge in RELION 3.1. The mask included the periplasmic scaffold and first ring of the basal disk, as the scaffold appears to attach onto it. This mask was used to computationally remove signal outside of the periplasmic regions of interest, as implemented in RELION 3.1. The signal subtraction and subsequent masked classification and refinement was conducted for the combined dataset, as well as K2 and F3 datasets separately. The highest resolution was reached with the merged data, the periplasmic scaffold map reaching 7.68 Å from 32,790 particles.

The periplasmic scaffold map was post-processed using LAFTER (71) as implemented in the CCP-EM 1.6.0 software suite (72) to suppress noise and enhance signal between the half-maps. The LAFTER-filtered map of the scaffold was used for docking and modelling of periplasmic regions.

The focused refinement of the stator complex used a hybrid workflow of RELION and CryoSPARC. Particles were imported into Relion and a 2D classification was run. Particles from the 2D classes were selected to run a 3D classification job. The selected particles were inputted into a Refine 3D job. A subtract job was run with a lathe mask masking out the stators (MotA and MotB), C-ring and PflB to subtract out the stators. A 3D classification job was then run with the same lathe mask around the stators. Particles were selected and refined in Refine3D. The already subtracted and refined particles were then imported into Cryosparc with the subtracted and refined volume from Relion as a template. A homogeneous refinement job was run which provided the final map of the stators with 17,753 particles and 15.95A resolution.

## Subtomogram averaging

Fiducial models were generated and tilt series were aligned for tomogram reconstruction using the IMOD package (73). Tomo3D (74) was used to reconstruct tomograms with the SIRT method. All steps were automated by in-house custom scripts.

Subtomogram averaging was performed using the Dynamo package (75). Motors were picked in IMOD and imported into Dynamo as 'oriented particles' using an in-house script, and subtomograms were extracted for averaging. For each structure, an initial model was obtained by reference-free averaging of the oriented particles, with randomized Z-axis rotation to alleviate missing wedge artefacts. This initial model was used for a first round of alignment and averaging steps, implementing an angular search and translational shifts, with cone diameter and shift limits becoming more stringent across iterations. The resulting average was used as a starting model for a round of masked alignment and averaging. In this round, custom alignment masks were implemented, focusing on the periplasmic and inner membrane-associated parts of the motor. This excluded dominant features that would otherwise drive the alignment, most prominently the outer membrane and extracellular hook. 17-fold rotational averaging was applied. The final $pflA_{\Delta 18\text{-}168}$ average was derived from 103 particles. The △*pflC* average from 101 particles, △*pflD* average from 195 particles, and the *flgQ-mCherry* average from 155 particles.

## Homology Modelling

Homology-modelled proteins in Table 1 were modelled in their monomeric forms using the SWISS-MODEL server (76,77). The sequence of each protein as it appears in *C. jejuni* strain 81-176 was first run through the SignalP 6.0 server (78) and any predicted signal sequences were trimmed away. The remaining 'mature' sequence was then input in alignment mode, and the best scoring hit was used as a template for modelling single chains. They were then assembled into appropriate multimers by aligning multiple copies of each protein against the template structure. In this way, we assembled 26-meric LP-ring model of FlgH and FlI, an arc of 4 FliL, a hexamer of $FlhA_C$, and the rod and FliPQR.

A 34-mer of FliF did not match the FliF density in our whole-motor map. The MS-ring in *C. jejuni* is wider, containing more FliF subunits. Extrapolating based on the diameters of FliF β-collars in *Salmonella* and *C. jejuni*, the *C. jejuni* FliF ring should have approximately ~40.6 subunits relative to *Salmonella*'s 34. Accommodating for inaccuracies in calculations, we modelled FliF β-collars of 39-44 subunits. This was implemented with Chimera scripts, ensuring a constant inter-subunit spacing. All six FliF multimers were docked into the

806 appropriate density with Chimera's 'Fit in Map' function, also used to measure the correlation
807 between the map and model. Best agreement was seen in the 41- 42- and 43-mer models.

808 Having determined the FliF stoichiometry at approximately 42, we modelled its ring-building
809 motifs (RBMs) 1 and 2. As in (37), we aligned pairs of domains to corresponding domains in
810 PrgK and PrgH (PDB 5TCP, (79)) to model RBM12 in the 'inner' and 'outer' conformations,
811 respectively. I modelled the inner ring as having 23 RBM1 and RBM2 domains in the 'inner'
812 conformation. The remaining 19 RBM12 domains were modelled in the 'outer' conformation,
813 evenly spaced.

814 **De novo Modelling**

815 ColabFold (39), the community-run implementation of Deepmind's AlphaFold2 (38) was
816 used to create structural models of PflA, PflB, a dimer of PflAB, PflC, PflD, FlgP (as a
817 monomer, trimer, and heptamer), $FlhA_N$, FlhB, and a dimer of $MotB_P$ (removed
818 transmembrane residues 1-67). PflA residues 16-455 and PflB residues 113-384 were used
819 to predict the structure of the PflAB dimerisation interface.

820 We assembled an $FlhA_N$ nonamer by predicting trimers using the ColabFold AlphaFold2
821 interface (38,39). Consistent with $FlhA_N$ forming a symmetric nonamer, the angle between
822 monomers corresponded to 40°. We iteratively aligned staggered trimers to arrive at a
823 nonamer.

824 **Flagellar motility assays**

825 WT *C. jejuni* and DAR2076 were grown from freezer stocks on MH agar containing
826 trimethoprim for 48 h in microaerobic conditions at 37 C. Strains were restreaked on MH
827 agar containing trimethoprim and grown for 16 h at 37 C in microaerobic conditions. After
828 growth, strains were resuspended from plates and diluted to an $OD_{600}$ 0.8. Strains were then
829 stabbed in MH motility agar (0.4% agar) and incubated at 37 C in microaerobic conditions for
830 30 h and assessed for migration from the point of inoculation.
831

832 **Docking and refinement**

833 Multimeric models of FliPQR-rod, FlhB, FlhA, LP-rings, and FliF models were rigidly docked
834 into the whole-motor map in UCSF ChimeraX 1.4 (80).

835 PflD, MotB, an arc of FliL, and MotA model taken from (33) were rigidly docked into the
836 LAFTER-filtered scaffold map. For regions where secondary structure was resolved, our
837 protein models were refined into the scaffold map using the ISOLDE (81) plugin in UCSF

Chimera X 1.4. The PflAB dimer was refined into the post-processed scaffold map in this way. AlphaFold2 models of FlgP multimers showed that each subunit interacts with subunits i−1 and i−2. To avoid artefacts due to this, a heptamer of FlgP was docked into the innermost basal disk ring and then refined into the map. Two subunits were then removed from each end, resulting in a fitted FlgP trimer. The PflC model was first separated into two domains, $PflC_N$ (residues 16-263) and $PflC_C$ (264-364). The linker (224-263) was pivoted into the appropriate density and the two domains re-merged. The resulting protein was then refined into the map.

Six copies of the refined $PflC_N$ structure were rigid-body docked into an asymmetric unit of PflC lattice of the medial disk. In the same way, we docked the structured C-terminal domain of PflC (residues 91-162) into the scaffold map.

**Plasmid construction and cloning in E. coli**

*C. jejuni* proteins for recombinant expression in *E. coli* were cloned into the pLIC plasmid backbone, which confers resistance to ampicillin and places the gene of interest under an IPTG-inducible T7 promoter for high levels of controlled expression. We used WT *C. jejuni* genomic DNA as template for gene amplification (extracted using the Wizard genomic DNA purification kit by Promega), and the Gibson Assembly method (82) to seamlessly assemble all plasmid constructs. For all constructs, primer pairs were designed to amplify 1) the pLIC backbone and 2) the gene to be expressed, while also introducing a 25~30 bp complementary overlap between the two fragments. The pLIC plasmid primers also introduced an N-terminal hexahistidine tag. After vector linearisation and purification of PCR product, it was digested with DpnI (New England Biolabs) to remove template vector.

The resulting linear DNA fragments were assembled using the Gibson Assembly master mix (New England Biolabs). 5 µL of mix was added to 15-20 fmol of linearised vector and 4× excess of insert and topped up to 10 µL with double-distilled water ($ddH_2O$). The tube was incubated at 50°C for 15 min and kept on ice until transformation.

Before transformation, 30 µL of $ddH_2O$ was added to the 10 µL reaction. 2 µL of diluted Gibson mix was added to 25 µL of chemically competent *E. coli* DH5α and transformed using the heat shock method (83). The entire volume of the tube was then plated onto a carbenicillin-supplemented LB agar plate.

After confirmation by Sanger sequencing (Source Bioscience), each assembled construct was isolated from the cloning strain (QIAprep Spin Miniprep Kit, QIAGEN) and transformed into E. coli BL21(DE3) for recombinant overexpression.

**Protein overexpression and purification**

All proteins encoded on pLIC expression vectors were purified using the same protocol. A small (5 mL) overnight liquid culture of *E. coli* BL21(DE3) carrying the appropriate expression vector was prepared and diluted 1:50 in 1000 mL of LB medium. Shaking at 37°C, the culture was grown to OD600 0.4-0.6, after which protein expression was induced by addition of 0.5 mM IPTG. Temperature was reduced to 18°C and protein was expressed overnight.

Cells were harvested at 5000 rpm, 4°C for 20 min. All subsequent steps were done on ice using buffers chilled to 4°C. The cell pellet was gently resuspended in ~35 mL of wash buffer (50 mM Tris-HCl, 100 mM NaCl, 30 mM imidazole, pH 7.5). DNase and protease inhibitor were added (cOmplete Protease Inhibitor Cocktail, Roche). Cells were lysed using a LM10 Microfluidizer Processor cell disrupter (Analytik) at 15,000 psi. Lysate was centrifuged at 17,000 rpm, 4°C for 30 min to pellet debris. The resulting supernatant was filtered through a 0.45 µm syringe filter (Whatman).

A 5 mL HisTrap HP affinity chromatography nickel column (Cytiva) was first equilibrated with wash buffer. Supernatant was loaded onto the column with a peristaltic pump at a flow rate of 3 mL/min. The column was washed with 50 mL of wash buffer and then transferred onto a Fast protein liquid chromatography system (BioRad). The column was further washed until the UV trace was flat. Then, protein was eluted from the column using a high-imidazole buffer (50 mM Tris-HCl, 100 mM NaCl, 500 mM imidazole, pH 7.5) at a flow of 2 mL/min using ‘reverse flow’.

The purified protein was kept at 4°C or flash-frozen in LN2 for longer-term storage before characterising them by mass photometry.

**Analytical SEC**

Analytical SEC of PflC and $PflC_N$ (△236-349) was performed with a ENrich SEC 650 column (Bio-Rad), equilibrated with 1× PBS at a flow rate of 0.1 ml min−1 and a total sample injection volume of 400 µl. The SEC column was calibrated using the Protein Standard Mix 15 – 600

kDa (Superdex #69385). Absorption was recorded at 280, 220 and 495nm to follow elution profiles and plotted using GraphPad Prism.

**Protein pulldowns**

**Co-immunoprecipitation (coIP) of PflA/B-3xFLAG with PflD-sfGFP, and PflC-3xFLAG**

Chromosomally epitope-tagged fusions of PflC-3xFLAG (CSS-4720) or PflA-3xFLAG and PflD-sfGFP (CSS-5714), and PflB-3xFLAG and PflD-sfGFP (CSS-5716) were used together with the untagged *C. jejuni* NCTC11168 WT (CSS-0032) and PflD-sfGFP only (CSS-4666) as controls for immunoprecipitation. Co-purification of FlgP or PflD-sfGFP was investigated by western blot (WB) analysis using FlgP specific antisera (21) or an anti-GFP antibody (Roche #11814460001, RRID:AB_390913), respectively. In brief, strains were grown to an $OD_{600}$ of 0.6 and 60 $OD_{600}$ of cells were harvested (5,000 rpm, 20 min, 4°C) and washed in buffer A (20 mM Tris-HCl pH 8, 1 mM $MgCl_2$, 150 mM KCl, 1 mM DTT). In parallel, 1 $OD_{600}$ of cells was harvested as “culture” control and boiled in 1 x protein loading buffer (PL; 62.5 mM Tris-HCl, pH 6.8, 100 mM DTT, 10% (v/v) glycerol, 2% (w/v) SDS, 0.01% (w/v) bromophenol blue; 8 min at 95°C, shaking at 1,000 rpm). Next, 60 $OD_{600}$ cell pellets were lysed with a FastPrep system (MP Biomedical, matrix B, 1 x 4 m/s, 10 s) in 1 ml lysis buffer [buffer A including 1 mM PMSF (phenylmethylsulfonyl fluoride, Roche), 20 U DNase I (Thermo Fisher Scientific), 200 U RNase Inhibitor (moloX, Berlin) and Triton X-100 (2 µl/ml lysis buffer)]. Cleared lysates (13,000 rpm, 10 min, 4°C) were incubated with 35 µl anti-FLAG antibody (Sigma-Aldrich, #F1804-1MG, RRID:AB_262044) for 30 min at 4°C with rotation. Before and after incubation, a 1 $OD_{600}$ aliquot was taken aside as lysate and supernatant 1 samples. Lysates with anti-FLAG antibody were then incubated for additional 30 min (4°C, rotating) with 75 µl/sample pre-washed (3 times in buffer A) Protein A-Sepharose beads (Sigma-Aldrich, #P6649). Afterwards, the supernatant/unbound fraction was removed after centrifugation (15,000 x g, 1 min, 4°C; supernatant 2) and Protein A-Sepharose beads with bound proteins were washed 5 times with buffer A. Elution of the bound proteins was performed with boiling of the beads in 400 µl 1 x PL (8 min at 95°C, 1,000 rpm). Six volumes of acetone were used to precipitate eluted proteins overnight at -20°C. Next, precipitated proteins were harvested by centrifugation (15,000 rpm, 1 h, 4°C), air-dried and resuspended in 1 x PL. Culture, lysate, supernatants 1 & 2, wash (aliquots corresponding to 0.1 $OD_{600}$) and eluate samples (corresponding to 10 $OD_{600}$) were analysed by WB. Western Blots were performed as described previously (60) and probed with the appropriate primary antibodies (anti-FLAG, anti-GFP (1:1,000 in 3% BSA/TBS-T)) or FlgP antisera (1:20,000 in 3% BSA/TBS-T) and secondary antibodies (anti-mouse or anti-rabbit

IgG, HRP-conjugate (1:10,000) in 3% BSA/TBS-T; GE Healthcare, #RPN4201 and #RPN4301, respectively).

**Mass Photometry**

Microscope coverslips (24 × 60 mm, Carl Roth) and CultureWell Gaskets (CW- 50R-1.0, 50-3 mm diameter × 1 mm depth) were cleaned with alternating dd$H_2O$ and 100% isopropanol washes, then dried roughly with pressurised air and left to dry further overnight at room temperature. Before use, gaskets were assembled onto coverslips and placed on the lens of a One$^{MP}$ mass photometer (Refeyn Ltd) with immersion oil.

For each measurement, a gasket was first filled with 18 µL of PBS buffer and the instrument was focused. Then, 2 µL of sample was added to the droplet and rapidly mixed by pipetting. Measurements were then started using AcquireMP v1.2.1 (Refeyn Ltd). For each measurement, data was acquired for 60 s at 100 frames per second. Mass photometry data was processed and analyzed in DiscoverMP software v.1.2.3 (Refeyn Ltd).

Measurements were conducted using affinity chromatography-purified proteins diluted to 200-800 nM, calculated from absorption at 280 nm. 2 µL of sample was added to 18 µL PBS droplet and mixed. For measurements of hetero-oligomers, the different proteins were first combined and mixed in a separate tube and subsequently applied to the PBS droplet. MP measurements were calibrated against molecular masses of commercial NativeMark$^{TM}$ unstained protein standard (Thermo Fisher Scientific). 1 µL of NativeMark$^{TM}$ was diluted 30-fold in PBS and 2 µL of this solution was added to 18 µL PBS for measurement. Detected peaks corresponded to 66 kDa, 146 kDa, 480 kDa, and 1048 kDa and were used to calibrate subsequent measurements in DiscoverMP.

**Construction of plasmids and strains for PflA and PlfB co-immunoprecipitation experiments**

Plasmids were constructed with specific promoters for expression of FLAG-tagged proteins in *C. jejuni* mutants for co-immunoprecipitation experiments. To express a C-terminal FLAG-tagged PflA protein, a 206-base pair DNA fragment from *C. jejuni* 81-176 that contained the promoter for *flaA* encoding the major flagellin with its start codon and an in-frame SpeI restriction site followed by an in-frame BamHI restriction site was amplified by PCR. This fragment was cloned into the XbaI and BamHI sites of pRY108 to result in pDAR1425. Primers were then constructed to amplify DNA from codon 2 to the penultimate codon of *pflA* from *C. jejuni* 81-176 with an in-frame C-terminal FLAG tag epitope and stop codon. This DNA fragment was then cloned into the BamHI site of pDAR1425 so that *pflA*-FLAG was expressed from the flaA promoter to create pDAR3417. As a control, a 229-base pair DNA

fragment from *C. jejuni* 81-176 that contained the promoter for *flaA* encoding the major flagellin with its start codon and DNA encoding an in-frame FLAG tag epitope followed by an in-frame BamHI restriction site was cloned into the XbaI and BamHI sites of pRY108 to create pDAR1604. pDAR1604 and pDAR3417 were then moved into DH5a/pRK212.1 for conjugation into DAR1124. Transconjugants were selected for on media with kanamycin and verified to contain the correct plasmids to result in DAR3447 and DAR3477.

To express a C-terminal FLAG-tagged PflB protein, primers were constructed to amplify DNA from codon 2 to the penultimate codon of pflB from *C. jejuni* 81-176 with an in-frame C-terminal FLAG tag epitope and stop codon. This DNA fragment was then cloned into the BamHI site of pECO102 so that pflB-FLAG was expressed from the cat promoter to create pDAR3414. pDAR965 and pDAR3414 were then moved into DH5a/pRK212.1 for conjugation into DAR981. Transconjugants were selected for on media containing chloramphenicol and verified to contain the correct plasmids to result in DAR3451 and DAR3479.

**PflA and PflB co-immunoprecipitation experiments**

*C. jejuni* Δ*pflA* and Δ*pflB* mutants containing plasmids to express a FLAG-tag alone or C-terminal FLAG-tagged PflA or PflB proteins were grown from freezer stocks on MH agar containing chloramphenicol for 48 h in microaerobic conditions at 37°C. Each strain was restreaked onto two MH agar plates containing chloramphenicol and grown for 16 h at 37°C in microaerobic conditions. After growth, strains were resuspended from plates in PBS and centrifuged for 10 min at 6000 rpm. Each cell pellet was resuspended in 2 ml of PBS. Formaldehyde was added to a final concentration of 0.1% and suspensions were gently mixed for 30 min at room temperature to crosslink proteins. After crosslinking, 0.4 ml of 1 M glycine was added to each sample and then suspensions were gently mixed for 10 min at room temperature to quench the crosslinking reaction. Bacterial cells were collected by centrifugation for 10 min at 6000 rpm. Cells were then disrupted by osmotic lysis and FLAG-tagged proteins with associated interacting proteins were immunoprecipitated with α-FLAG M2 affinity resin as previously described (56,84).

To identify potential proteins interacting with PflA and PflB, resin with immunoprecipitated proteins were resuspended in SDS-loading buffer and electrophoresed on a 4-20% TGX stain-free gel (Bio-Rad) for 10 min. The gel was then stained with Coomassie blue for 30 min and then destained overnight. After equilibration of the gel in $dH_2O$ for 30 min, a 1 cm region of the gel containing a majority of the co-immunoprecipitated proteins was excised and diced into 1 mm pieces and then submitted for analysis by LC-MS/MS. After identification of proteins that co-immunoprecipitated with the FLAG-tagged bait protein and with the resin

1001 from the FLAG-tag only sample (the negative control), a ratio for each protein was
1002 determined by dividing the abundance of each protein detected in the FLAG-tagged bait
1003 protein sample by the abundance of each protein in the negative control. The top twenty
1004 proteins with the highest ratios for co-immunoprecipitation with the FLAG-tagged bait
1005 proteins are reported. The top twenty proteins that only co-immunoprecipitated with the
1006 FLAG-tagged bait proteins and were not detected in the negative control samples are also
1007 reports with their respective raw abundance counts.

# Supplemental information titles and legends

**Figure S1: Flowchart and resolution estimates of structure determination of the Campylobacter jejuni bacterial flagellar motor using in situ single particle analysis. (A) Simplified flowchart showing the generation of cryoEM volumes. (B) Central slice through the refined whole-motor structure. (C) FSC curve for B. (D) and (E) show slices through the volume of the refined, signal-subtracted periplasmic scaffold. (F) FSC curve for DE.**

**Figure S2: FlgP is a modified SHS2 fold that enables oligomerisation in the basal disk. (A) AlphaFold2 model of FlgP (signal sequence removed, sites 1-16). The N-terminal unstructured linker is followed by a SHS2 domain, modified with a β-hairpin and short C-terminal helix. (B) AlphaFold model of FlgQ (signal sequence removed). The double β-hairpin resembles a two-protomer repeat of FlgP. (C) Tagging FlgQ with mCherry, the resulting motor is indistinguishable from WT (1). (D) Dodecin exemplifies the core SHS2 fold (PDBID: 1MOG). (E) Left: 17 FlgP trimers docked and refined into the scaffold map. Right: Close-up of a FlgP triplet, subunits interlocking by β-hairpin interactions.**

**Figure S3: PflC and PflD interact with known flagellar disk structure components. (A) Western blot analysis of coIP experiment of PflC-3xFLAG. As control, untagged wild-type cells (WT) were used. Detected heavy (HC) and light (LC) antibody chains are indicated. C: culture; L: lysate. (B) Western blot analysis of coIP experiment of PflA-3xFLAG, PflD-sfGFP double tagged strain. As controls, PflD-sfGFP and untagged wild-type (WT) cells were used. Detected heavy (HC) antibody chains are indicated. C: culture; L: lysate; Sn1/2: supernatant 1/2; W: wash; E: eluate. (C) Western analysis of coIP experiment of PflB-3xFLAG, PflD-sfGFP double tagged strain. As controls, PflD-sfGFP and untagged wild-type cells were used. Detected heavy (HC) antibody chains are indicated. C: culture; L: lysate; Sn1/2: supernatant 1/2;W: wash; E: eluate.**

**Figure S4: PflC (a previously unknown glycoprotein) resembles HtrA lacking its conserved serine protease active site. (A) Top-down view of the medial disk with docked $PflC_N$ subunits. (B) Unaccounted-for density is present at N239 (red atoms) of every PflC. Similar to the known glycans on PflA, this likely corresponds to previously uncharacterised glycosylation. (C) The His-Asp-Ser catalytic triad in the protease domain of HtrA (green) is not conserved in PflC (pink). (HtrA PDB ID 6Z05).**

**Figure S5: PflC oligomerises in vitro and this interaction increases upon removal of its C-terminal PDZ domain. (A) Size Exclusion Chromatography of PflC (red) along with protein standards (grey) showing elution volume. (B) Calibration graph showing a dimer of PflC (red) corresponding to retention times during elution. (C) Mass photometry measurements of purified PflC (replicates). (D) Size Exclusion Chromatography of $PflC_N$ (Δ236-349, green) along with protein standards (grey) showing elution volume. (E) Calibration graph of $PflC_N$ (green) corresponding to retention times during elution. (F) Mass photometry measurements of purified $PflC_N$. Theoretical masses are shown in the inserts. The instrument's limit of detection is 35 kDA, meaning the monomer mass is larger than otherwise expected.**

**Figure S6: Mass photometry shows that PflA dimerises with PflB via its N-terminal β-sandwich domain. (A-D) Mass photometry measurements of purified PflA and PflB constructs show the proteins are mainly monodisperse. There is a dimer peak present for the PflAΔCter construct, likely due to a reduced stability and solubility. (E-G) Mass photometry measurements of mixtures of PflB and PflA variants. Dimer peaks appear only when β-sandwich and linker domain of PflA is present. In panels E and G, monomer peaks of PflA and PflB are not resolved due to their similar molecular weights. In the bottom panel, the 54 kDa peak corresponds to PflAΔCter, and the 79 kDa peak to PflB. Monomer peaks have a yellow background, dimer peaks red.**

**Figure S7: Possible contact sites between MotB and PflAB of the periplasmic scaffold. (A) A region on the surface of PflB (shown in surface representation) appears likely to be involved in binding MotB stalk. This region corresponds to four surface-exposed α-helices. (B) These helices are positioned close to unaccounted density that's stemming from these regions and towards the PGB domain of MotB. (C) The four helices (marked in cyan) are at positions Y360-D382 for H1 and H2, P760-T773 for H3, and V791-T803 for H4. (D) A PflA helix (K307-N320) could also be involved in stator recruitment, here shown with side chains in stick form.**

**Figure S8. Deletion of fliL has only a minor effect on motility. A representative motility agar plate stabbed with WT and fliL::cat demonstrates that fliL knockout has only a minor effect on motility.**

**Figure S9: Validation of those protein chains modelled in the scaffold map to subnanometre resolution. (A) Map-model FSC curves for protein models refined into the scaffold map: FlgP, PflA, PflC1, and PflC2-7, as calculated with phenix.mtriage. (B) Cross-correlation per residue plots of proteins docked into the map: PflB, FliL, MotB, PflD, calculated in phenix.**

**Table S1: PflA and PflB pulldowns and mass spectrometry**

**Table S2: Structural components of the C. jejuni flagellar motor**

# References

1. Johnson AD. The rewiring of transcription circuits in evolution. *Evolutionary genetics*. 2017;47: 121–127. https://doi.org/10.1016/j.gde.2017.09.004.
2. Bridgham JT, Carroll SM, Thornton JW. Evolution of Hormone-Receptor Complexity by Molecular Exploitation. *Science (80-. ).* 2006;312(5770): 97 LP – 101. https://doi.org/10.1126/science.1123348.
3. Finnigan GC, Hanson-Smith V, Stevens TH, Thornton JW. Evolution of increased complexity in a molecular machine. *Nature*. 2012;481(7381): 360–364. https://doi.org/10.1038/nature10724.
4. Pillai AS, Chandler SA, Liu Y, Signore AV, Cortez-Romero CR, Benesch JLP, et al. Origin of complexity in haemoglobin evolution. *Nature*. 2020;581(7809): 480–485. https://doi.org/10.1038/s41586-020-2292-y.
5. Schulz L, Guo Z, Zarzycki J, Steinchen W, Schuller JM, Heimerl T, et al. Evolution of increased complexity and specificity at the dawn of form I Rubiscos. *Science*. 2022;378(6616): 155–160. https://doi.org/10.1126/science.abq1416.
6. Beeby M, Ferreira JL, Tripp P, Albers SV, Mitchell DR. Propulsive nanomachines: the convergent evolution of archaella, flagella and cilia. *FEMS microbiology reviews*. 2020;44(3): 253–304. https://doi.org/10.1093/femsre/fuaa006.
7. Chen S, Beeby M, Murphy GE, Leadbetter JR, Hendrixson DR, Briegel A, et al. Structural diversity of bacterial flagellar motors. *EMBO J.* 2011;30(14): 2972–2981. https://doi.org/10.1038/emboj.2011.186.
8. Terashima H, Fukuoka H, Yakushi T, Kojima S, Homma M. The Vibrio motor proteins, MotX and MotY, are associated with the basal body of Na+-driven flagella and required for stator formation. *Mol. Microbiol.* 2006;62(4): 1170–1180. https://doi.org/10.1111/j.1365-2958.2006.05435.x.
9. Beeby M, Ribardo DA, Brennan CA, Ruby EG, Jensen GJ, Hendrixson DR. Diverse high-torque bacterial flagellar motors assemble wider stator rings using a conserved protein scaffold. *Proc. Natl. Acad. Sci.* 2016;113(13): E1917–E1926. https://doi.org/10.1073/pnas.1518952113.
10. Chaban B, Coleman I, Beeby M. Evolution of higher torque in Campylobacter-Type bacterial flagellar motors. *Sci. Rep.* 2018;8(1): 1–11. https://doi.org/10.1038/s41598-017-18115-1.
11. Beeby M. Motility in the epsilon-proteobacteria. *Curr. Opin. Microbiol.* 2015;28: 115–121. https://doi.org/10.1016/J.MIB.2015.09.005.
12. Chang Y, Zhang K, Carroll BL, Zhao X, Charon NW, Norris SJ, et al. Molecular mechanism for rotational switching of the bacterial flagellar motor. *Nature Structural & Molecular Biology*. 2020;27(11): 1041–1047. https://doi.org/10.1038/s41594-020-0497-2.
13. Tachiyama S, Skaar R, Chang Y, Carroll BL, Muthuramalingam M, Whittier SK, et al. Composition and Biophysical Properties of the Sorting Platform Pods in the Shigella

Type III Secretion System. *Frontiers in Cellular and Infection Microbiology*. 2021;11. https://www.frontiersin.org/articles/10.3389/fcimb.2021.682635

14. Johnson S, Furlong EJ, Deme JC, Nord AL, Caesar JJE, Chevance FFV, et al. Molecular structure of the intact bacterial flagellar basal body. *Nature Microbiology*. 2021; https://doi.org/10.1038/s41564-021-00895-y.
15. Tan J, Zhang X, Wang X, Xu C, Chang S, Wu H, et al. Structural basis of assembly and torque transmission of the bacterial flagellar motor. *Cell*. 2021;184(10): 2665-2679.e19. https://doi.org/10.1016/j.cell.2021.03.057.
16. Liu Y, Sigworth FJ. Automatic cryo-EM particle selection for membrane proteins in spherical liposomes. *Journal of Structural Biology*. 2014;185(3): 295–302. https://doi.org/10.1016/j.jsb.2014.01.004.
17. Tonggu L, Wang L. Structure of the Human BK Ion Channel in Lipid Environment. *Membranes*. 2022;12(8): 758. https://doi.org/10.3390/membranes12080758.
18. Kawamoto A, Morimoto YV, Miyata T, Minamino T, Hughes KT, Kato T, et al. Common and distinct structural features of Salmonella injectisome and flagellar basal body. *Scientific Reports*. 2013;3(1): 3369. https://doi.org/10.1038/srep03369.
19. Balaban M, Hendrixson DR. Polar Flagellar Biosynthesis and a Regulator of Flagellar Number Influence Spatial Parameters of Cell Division in Campylobacter jejuni. *PLOS Pathogens*. 2011;7(12): e1002420. https://doi.org/10.1371/journal.ppat.1002420.
20. Butan C, Lara-Tejero M, Li W, Liu J, Galán JE. High-resolution view of the type III secretion export apparatus in situ reveals membrane remodeling and a secretion pathway. *Proceedings of the National Academy of Sciences*. 2019;116(49): 24786–24795. https://doi.org/10.1073/pnas.1916331116.
21. Sommerlad SM, Hendrixson DR. Analysis of the roles of FlgP and FlgQ in flagellar motility of Campylobacter jejuni. *J. Bacteriol.* 2007;189(1): 179–186. https://doi.org/10.1128/JB.01199-06.
22. Bieger B, Essen LO, Oesterhelt D. Crystal Structure of Halophilic Dodecin: A Novel, Dodecameric Flavin Binding Protein from Halobacterium salinarum. *Structure*. 2003;11(4): 375–385. https://doi.org/10.1016/S0969-2126(03)00048-0.
23. Vallese F, Mishra NM, Pagliari M, Berto P, Codolo G, de Bernard M, et al. Helicobacter pylori antigenic Lpp20 is a structural homologue of Tipα and promotes epithelial-mesenchymal transition. *Biochimica et Biophysica Acta (BBA) - General Subjects*. 2017;1861(12): 3263–3271. https://doi.org/10.1016/j.bbagen.2017.09.017.
24. Holm L. Dali server: structural unification of protein families. *Nucleic Acids Research*. 2022;50(W1): W210–W215. https://doi.org/10.1093/nar/gkac387.
25. Zarzecka U, Grinzato A, Kandiah E, Cysewski D, Berto P, Skorko-Glonek J, et al. Functional analysis and cryo-electron microscopy of Campylobacter jejuni serine protease HtrA. *Gut Microbes*. 2020;12(1): 1810532. https://doi.org/10.1080/19490976.2020.1810532.
26. Harris BZ, Lim WA. Mechanism and role of PDZ domains in signaling complex assembly. *Journal of Cell Science*. 2001;114(18): 3219.
27. Lee HJ, Zheng JJ. PDZ domains and their binding partners: structure, specificity, and modification. *Cell Communication and Signaling*. 2010;8(1): 8. https://doi.org/10.1186/1478-811X-8-8.
28. Blatch GL, Lässle M. The tetratricopeptide repeat: a structural motif mediating protein-protein interactions. *BioEssays*. 1999;21(11): 932–939. https://doi.org/10.1002/(SICI)1521-1878(199911)21:11<932::AID-BIES5>3.0.CO;2-N.
29. D'Andrea LD, Regan L. TPR proteins: the versatile helix. *Trends Biochem. Sci.* 2003;28(12): 655–662. https://doi.org/10.1016/J.TIBS.2003.10.007.
30. Gao B, Lara-Tejero M, Lefebre M, Goodman AL, Galán JE. Novel Components of the Flagellar System in Epsilonproteobacteria. *MBio*. 2014;5(3): e01349-14. https://doi.org/10.1128/MBIO.01349-14.
31. Scott NE, Parker BL, Connolly AM, Paulech J, Edwards AVG, Crossett B, et al. Simultaneous glycan-peptide characterization using hydrophilic interaction

chromatography and parallel fragmentation by CID, higher energy collisional dissociation, and electron transfer dissociation MS applied to the N-linked glycoproteome of Campylobacter jejuni. *Molecular & cellular proteomics□: MCP*. 2010/04/01 ed. 2011;10(2): M000031-MCP201. https://doi.org/10.1074/mcp.M000031-MCP201.

32. Tachiyama S, Chan KL, Liu X, Hathroubi S, Li W, Peterson B, et al. The flagellar motor protein FliL forms a scaffold of circumferentially positioned rings required for stator activation. *Proceedings of the National Academy of Sciences*. 2022;119(4): e2118401119. https://doi.org/10.1073/pnas.2118401119.
33. Santiveri M, Roa-Eguiara A, Kühne C, Wadhwa N, Hu H, Berg HC, et al. Structure and Function of Stator Units of the Bacterial Flagellar Motor. *Cell*. 2020;183(1): 244-257.e16. https://doi.org/10.1016/j.cell.2020.08.016.
34. Guo S, Xu H, Chang Y, Motaleb MA, Liu J. FliL ring enhances the function of periplasmic flagella. *Proceedings of the National Academy of Sciences*. 2022;119(11): e2117245119. https://doi.org/10.1073/pnas.2117245119.
35. Lee LK, Ginsburg MA, Crovace C, Donohoe M, Stock D. Structure of the torque ring of the flagellar motor and the molecular basis for rotational switching. *Nature*. 2010;466(7309): 996–1000. https://doi.org/10.1038/nature09300.
36. Lynch MJ, Levenson R, Kim EA, Sircar R, Blair DF, Dahlquist FW, et al. Co-Folding of a FliF-FliG Split Domain Forms the Basis of the MS:C Ring Interface within the Bacterial Flagellar Motor. *Structure*. 2017;25(2): 317–328. https://doi.org/10.1016/j.str.2016.12.006.
37. Takekawa N, Kawamoto A, Sakuma M, Kato T, Kojima S, Kinoshita M, et al. Two Distinct Conformations in 34 FliF Subunits Generate Three Different Symmetries within the Flagellar MS-Ring. *mBio*. 2021;12(2): e03199-20. https://doi.org/10.1128/mBio.03199-20.
38. Jumper J, Evans R, Pritzel A, Green T, Figurnov M, Ronneberger O, et al. Highly accurate protein structure prediction with AlphaFold. *Nature*. 2021;596(7873): 583–589. https://doi.org/10.1038/s41586-021-03819-2.
39. Mirdita M, Schütze K, Moriwaki Y, Heo L, Ovchinnikov S, Steinegger M. *ColabFold - Making protein folding accessible to all*. 2022 Feb [Accessed 21st March 2022]. p. 2021.08.15.456425. https://doi.org/10.1101/2021.08.15.456425. [Accessed 21st March 2022].
40. Lensink MF, Brysbaert G, Mauri T, Nadzirin N, Velankar S, Chaleil RAG, et al. Prediction of protein assemblies, the next frontier: The CASP14-CAPRI experiment. *Proteins: Structure, Function, and Bioinformatics*. 2021;89(12): 1800–1823. https://doi.org/10.1002/prot.26222.
41. Katchalski-Katzir E, Shariv I, Eisenstein M, Friesem AA, Aflalo C, Vakser IA. Molecular surface recognition: determination of geometric fit between proteins and their ligands by correlation techniques. *Proceedings of the National Academy of Sciences*. 1992;89(6): 2195–2199. https://doi.org/10.1073/pnas.89.6.2195.
42. Terashima H, Li N, Sakuma M, Koike M, Kojima S, Homma M, et al. Insight into the assembly mechanism in the supramolecular rings of the sodium-driven Vibrio flagellar motor from the structure of FlgT. *PNAS*. 2013;110(15): 6133–6138. https://doi.org/10.1073/pnas.1222655110.
43. Engelhardt H, Schuster SC, Baeuerlein E. An archimedian spiral: The basal disk of the Wolinella flagellar motor. *Science (80-. ).* 1993;262(5136): 1046–1048. https://doi.org/10.1126/science.8235620.
44. Skórko-Glonek J, Wawrzynów A, Krzewski K, Kurpierz K, Lipińska B. Site-directed mutagenesis of the HtrA(DegP) serine protease, whose proteolytic activity is indispensable for Escherichia coli survival at elevated temperatures. *Gene*. 1995;163(1): 47–52. https://doi.org/10.1016/0378-1119(95)00406-V.
45. Krachler AM, Sharma A, Cauldwell A, Papadakos G, Kleanthous C. TolA Modulates the Oligomeric Status of YbgF in the Bacterial Periplasm. *Journal of Molecular Biology*.

2010;403(2): 270–285. https://doi.org/10.1016/j.jmb.2010.08.050.
46. Mandela E, Stubenrauch CJ, Ryoo D, Hwang H, Cohen EJ, Torres VL, et al. Adaptation of the periplasm to maintain spatial constraints essential for cell envelope processes and cell viability. Levin PA, Kana BD, Daley DO (eds.) *eLife*. 2022;11: e73516. https://doi.org/10.7554/eLife.73516.
47. Turner RD, Hurd AF, Cadby A, Hobbs JK, Foster SJ. Cell wall elongation mode in Gram-negative bacteria is determined by peptidoglycan architecture. *Nature Communications*. 2013;4(1): 1496. https://doi.org/10.1038/ncomms2503.
48. Nirody JA, Berry RM, Oster G. The Limiting Speed of the Bacterial Flagellar Motor. *Biophysical Journal*. 2016;111(3): 557–564. https://doi.org/10.1016/j.bpj.2016.07.003.
49. Sato K, Nakamura S, Kudo S, Toyabe S. Evaluation of the Duty Ratio of the Bacterial Flagellar Motor by Dynamic Load Control. *Biophysical Journal*. 2019;116(10): 1952–1959. https://doi.org/10.1016/j.bpj.2019.04.004.
50. Johnson S, Kuhlen L, Deme JC, Abrusci P, Lea SM. The Structure of an Injectisome Export Gate Demonstrates Conservation of Architecture in the Core Export Gate between Flagellar and Virulence Type III Secretion Systems. *mBio*. 2019;10(3). https://doi.org/10.1128/mBio.00818-19.
51. Taylor WR, Matthews-Palmer TRS, Beeby M. Molecular Models for the Core Components of the Flagellar Type-III Secretion Complex. Bhattacharjya S (ed.) *PLoS One*. 2016;11(11): e0164047. https://doi.org/10.1371/journal.pone.0164047.
52. Abrusci P, Vergara-Irigaray M, Johnson S, Beeby MD, Hendrixson DR, Roversi P, et al. Architecture of the major component of the type III secretion system export apparatus. *Nature Structural & Molecular Biology*. 2013;20(1): 99–104. https://doi.org/10.1038/nsmb.2452.
53. Hendrixson DR, Akerley BJ, DiRita VJ. Transposon mutagenesis of Campylobacter jejuni identifies a bipartite energy taxis system required for motility. *Molecular Microbiology*. 2001;40(1): 214–224. https://doi.org/10.1046/j.1365-2958.2001.02376.x.
54. Yao R, Alm RA, Trust TJ, Guerry P. Construction of new Campylobacter cloning vectors and a new mutational cat cassette. *Gene*. 1993;130(1): 127–130. https://doi.org/10.1016/0378-1119(93)90355-7.
55. Wiesner RS, Hendrixson DR, DiRita VJ. Natural Transformation of Campylobacter jejuni Requires Components of a Type II Secretion System. *Journal of Bacteriology*. 2003;185(18): 5408–5418. https://doi.org/10.1128/jb.185.18.5408-5418.2003.
56. Boll JM, Hendrixson DR. A Regulatory Checkpoint during Flagellar Biogenesis in Campylobacter jejuni Initiates Signal Transduction To Activate Transcription of Flagellar Genes. *mBio*. 2013;4(5): 10.1128/mbio.00432-13. https://doi.org/10.1128/mbio.00432-13.
57. Luethy PM, Huynh S, Parker CT, Hendrixson DR. Analysis of the Activity and Regulon of the Two-Component Regulatory System Composed by Cjj81176_1484 and Cjj81176_1483 of Campylobacter jejuni. *Journal of Bacteriology*. 2015;197(9): 1592–1605. https://doi.org/10.1128/jb.02564-14.
58. Cohen EJ, Nakane D, Kabata Y, Hendrixson DR, Nishizaka T, Beeby M. Campylobacter jejuni motility integrates specialized cell shape, flagellar filament, and motor, to coordinate action of its opposed flagella. *PLOS Pathogens*. 2020;16(7): e1008620. https://doi.org/10.1371/journal.ppat.1008620.
59. Van Vliet AHM, Wood AC, Wooldridge K, Ketley JM, Henderson J. 7.7 Genetic Manipulation of Enteric Campylobacter Species. In: Williams P, Ketley J, Salmond G (eds.) *Methods in Microbiology*. Academic Press; 1998. p. 407–419. https://doi.org/10.1016/S0580-9517(08)70301-5. [Accessed 2nd November 2022].
60. Dugar G, Svensson SL, Bischler T, Wäldchen S, Reinhardt R, Sauer M, et al. The CsrA-FliW network controls polar localization of the dual-function flagellin mRNA in Campylobacter jejuni. *Nature Communications*. 2016;7(1): 11667. https://doi.org/10.1038/ncomms11667.
61. Alzheimer M, Svensson SL, König F, Schweinlin M, Metzger M, Walles H, et al. A

three-dimensional intestinal tissue model reveals factors and small regulatory RNAs important for colonization with Campylobacter jejuni. Gaynor EC (ed.) *PLOS Pathog.* 2020;16(2): e1008304. https://doi.org/10.1371/journal.ppat.1008304.

62. Dugar G, Leenay RT, Eisenbart SK, Bischler T, Aul BU, Beisel CL, et al. CRISPR RNA-Dependent Binding and Cleavage of Endogenous RNAs by the Campylobacter jejuni Cas9. *Molecular Cell*. 2018;69(5): 893-905.e7. https://doi.org/10.1016/j.molcel.2018.01.032.
63. Corcoran CP, Podkaminski D, Papenfort K, Urban JH, Hinton JCD, Vogel J. Superfolder GFP reporters validate diverse new mRNA targets of the classic porin regulator, MicF RNA. *Molecular Microbiology*. 2012;84(3): 428–445. https://doi.org/10.1111/j.1365-2958.2012.08031.x.
64. Zheng SQ, Palovcak E, Armache JP, Verba KA, Cheng Y, Agard DA. MotionCor2: anisotropic correction of beam-induced motion for improved cryo-electron microscopy. *Nature Methods*. 2017;14(4): 331–332. https://doi.org/10.1038/nmeth.4193.
65. Scheres SHW. RELION: Implementation of a Bayesian approach to cryo-EM structure determination. *Journal of Structural Biology*. 2012;180(3): 519–530. https://doi.org/10.1016/j.jsb.2012.09.006.
66. Zivanov J, Nakane T, Forsberg BO, Kimanius D, Hagen WJ, Lindahl E, et al. New tools for automated high-resolution cryo-EM structure determination in RELION-3. Egelman EH, Kuriyan J (eds.) *eLife*. 2018;7: e42166. https://doi.org/10.7554/eLife.42166.
67. Rohou A, Grigorieff N. CTFFIND4: Fast and accurate defocus estimation from electron micrographs. *J. Struct. Biol.* 2015;192(2): 216–221. https://doi.org/10.1016/J.JSB.2015.08.008.
68. Pettersen EF, Goddard TD, Huang CC, Couch GS, Greenblatt DM, Meng EC, et al. UCSF Chimera—A visualization system for exploratory research and analysis. *Journal of Computational Chemistry*. 2004;25(13): 1605–1612. https://doi.org/10.1002/jcc.20084.
69. Goddard TD, Huang CC, Ferrin TE. Visualizing density maps with UCSF Chimera. *Journal of Structural Biology*. 2007;157(1): 281–287. https://doi.org/10.1016/j.jsb.2006.06.010.
70. Pintilie GD, Zhang J, Goddard TD, Chiu W, Gossard DC. Quantitative analysis of cryo-EM density map segmentation by watershed and scale-space filtering, and fitting of structures by alignment to regions. *Journal of Structural Biology*. 2010;170(3): 427–438. https://doi.org/10.1016/j.jsb.2010.03.007.
71. Ramlaul K, Palmer CM, Aylett CHS. A Local Agreement Filtering Algorithm for Transmission EM Reconstructions. *Journal of Structural Biology*. 2019;205(1): 30–40. https://doi.org/10.1016/j.jsb.2018.11.011.
72. Burnley T, Palmer CM, Winn M. Recent developments in the CCP-EM software suite. *Acta Crystallographica Section D: Structural Biology*. 2017;73(6): 469–477. https://doi.org/10.1107/S2059798317007859.
73. Kremer JR, Mastronarde DN, McIntosh JR. Computer visualization of three-dimensional image data using IMOD. *J. Struct. Biol.* 1996;116(1): 71–76. https://doi.org/10.1006/jsbi.1996.0013.
74. Agulleiro JI, Fernandez JJ. Tomo3D 2.0 - exploitation of advanced vector eXtensions (AVX) for 3D reconstruction. *J. Struct. Biol.* 2015;189(2): 147–152. https://doi.org/10.1016/j.jsb.2014.11.009.
75. Castaño-Díez D, Kudryashev M, Arheit M, Stahlberg H. Dynamo: A flexible, user-friendly development tool for subtomogram averaging of cryo-EM data in high-performance computing environments. *J. Struct. Biol.* 2012;178(2): 139–151. https://doi.org/10.1016/J.JSB.2011.12.017.
76. Waterhouse A, Bertoni M, Bienert S, Studer G, Tauriello G, Gumienny R, et al. SWISS-MODEL: homology modelling of protein structures and complexes. *Nucleic Acids Research*. 2018;46(W1): W296–W303. https://doi.org/10.1093/nar/gky427.
77. Studer G, Tauriello G, Bienert S, Biasini M, Johner N, Schwede T. ProMod3—A

versatile homology modelling toolbox. *PLOS Computational Biology*. 2021;17(1): e1008667. https://doi.org/10.1371/journal.pcbi.1008667.

78. Teufel F, Almagro Armenteros JJ, Johansen AR, Gíslason MH, Pihl SI, Tsirigos KD, et al. SignalP 6.0 predicts all five types of signal peptides using protein language models. *Nature Biotechnology*. 2022;40(7): 1023–1025. https://doi.org/10.1038/s41587-021-01156-3.
79. Worrall LJ, Hong C, Vuckovic M, Deng W, Bergeron JRC, Majewski DD, et al. Near-atomic-resolution cryo-EM analysis of the Salmonella T3S injectisome basal body. *Nature*. 2016;540(7634): 597–601. https://doi.org/10.1038/nature20576.
80. Pettersen EF, Goddard TD, Huang CC, Meng EC, Couch GS, Croll TI, et al. UCSF ChimeraX: Structure visualization for researchers, educators, and developers. *Protein Science*. 2021;30(1): 70–82. https://doi.org/10.1002/pro.3943.
81. Croll TI. ISOLDE: a physically realistic environment for model building into low-resolution electron-density maps. *Acta Crystallographica Section D: Structural Biology*. 2018;74(6): 519–530. https://doi.org/10.1107/S2059798318002425.
82. Gibson DG, Young L, Chuang RY, Venter JC, Hutchison CA, Smith HO. Enzymatic assembly of DNA molecules up to several hundred kilobases. *Nature Methods*. 2009;6(5): 343–345. https://doi.org/10.1038/nmeth.1318.
83. Froger A, Hall JE. Transformation of Plasmid DNA into E. coli Using the Heat Shock Method. *J. Vis. Exp.* 2007; e253. https://doi.org/10.3791/253.
84. Johnson TL, Scott ME, Sandkvist M. Mapping Critical Interactive Sites within the Periplasmic Domain of the Vibrio cholerae Type II Secretion Protein EpsM. *Journal of Bacteriology*. 2007;189(24): 9082–9089. https://doi.org/10.1128/jb.01256-07.

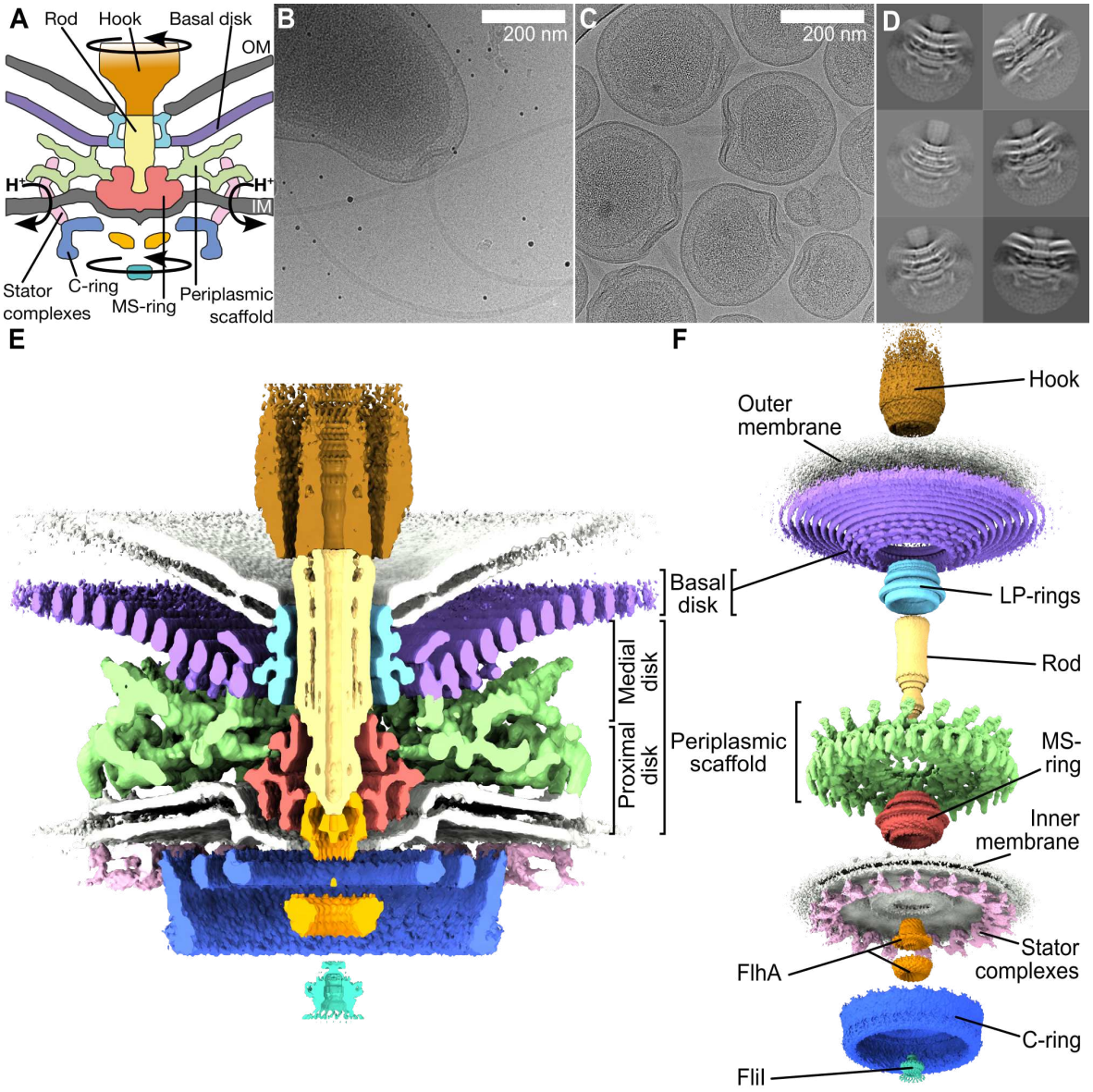


**Figure 1.**

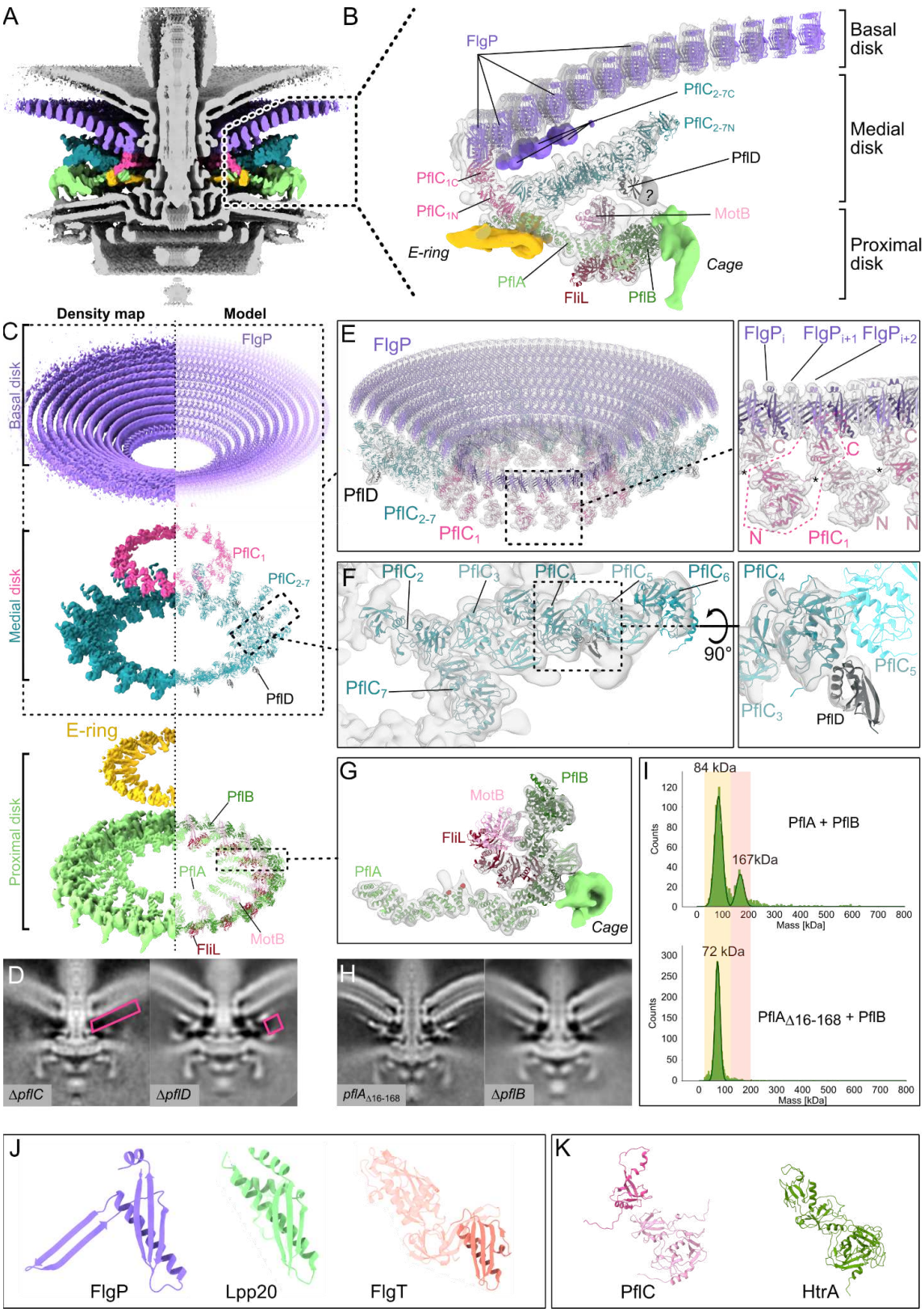


Figure 2.

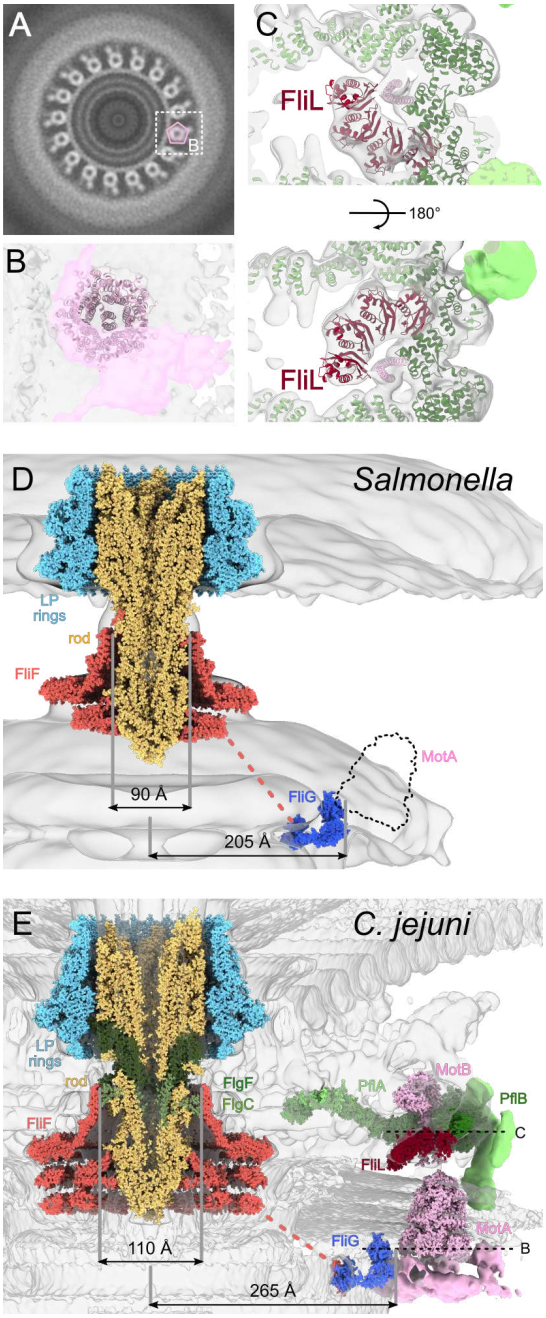


Figure 3.

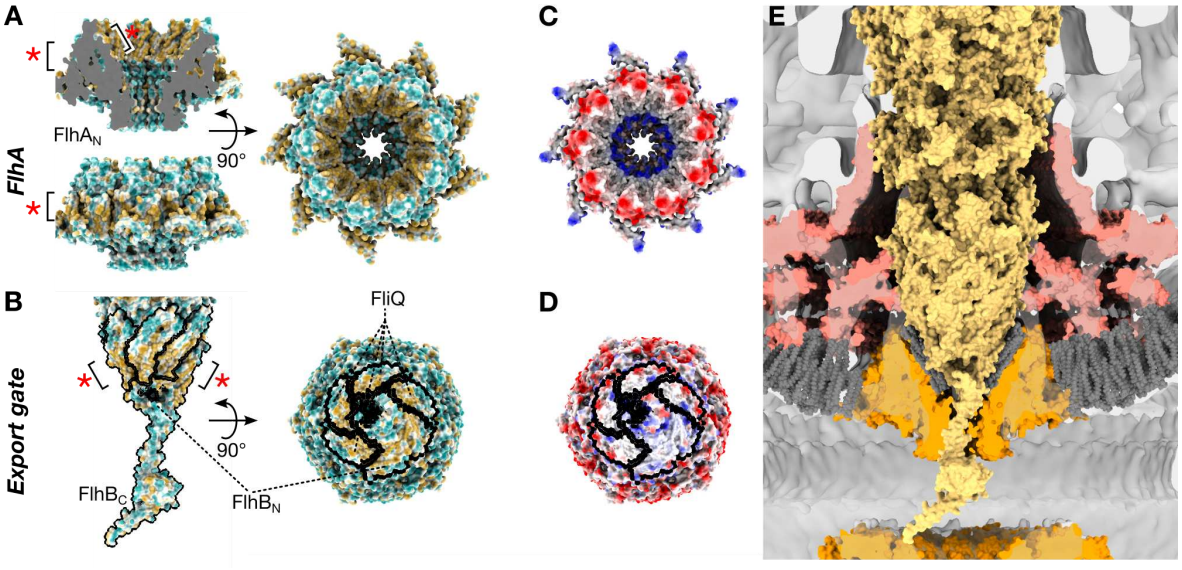


Figure 4.